A Smart Monitoring System for Bearing Fault Detection

By:

Xing Xing

A thesis presented to Lakehead University in fulfillment of the thesis
requirement for the degree of Master of Science in Electrical and Computer Engineering

Lakehead University, Thunder Bay, Ontario, Canada

Abstract

Rolling element bearings are commonly used in rotating machinery to support shafts, reduce friction, and increase power transmission efficiency. For a machinery system, bearing fault could be the most possible cause of mechanical failures. If bearing defect can be detected at its early stage, mechanical performance degradation and even economic losses can be avoided. Although many signal processing techniques have been proposed in the literature for bearing fault detection, reliable bearing fault diagnosis is still a challenging task in this R&D field, especially in industrial applications. The objective of this work is to develop a smart condition monitoring system and a signal processing technique for bearing fault detection. Firstly, a Field Programmable Gate Arrays (FPGA) based sinusoidal generator is developed to generate controllable sinusoidal waveforms and explore FPGA's potential applications in a data acquisition system to collect vibration signals. Secondly, an adaptive variational mode decomposition (AVMD) technique is proposed for bearing fault detection. The AVMD includes several steps in processing: 1) Signal characteristics are analyzed to determine the signal center frequency and the related parameters. 2) The ensemble-kurtosis index is suggested to select the optimal intrinsic mode function (IMF) to decompose the target signal. 3) The envelope spectrum analysis is performed using the selected IMF to identify the representative features for bearing fault detection. The effectiveness of the proposed AVMD technique is examined by simulation and experimental tests under different bearing conditions, with the comparison of other related bearing fault techniques.

Acknowledgements

After two years of study, my life as a master student is nearing its end. I could not have gotten this far without the help from my advisor and many individuals during past period of time.

First and foremost, I am grateful to my Supervisor, Dr. Wilson Wang for his patience guidance, constant support, and encouragement. I sincerely appreciate his help in my academic research and providing me with an excellent research platform for exploration in the academic field.

I would like to express my gratitude toward to Dr. Jian Deng from Civil Engineering and Dr. Qiang Wei from Electrical Engineering for reviewing this thesis, as well as Dr. Yushi Zhou for the guidance as the program coordinator.

I would also like to thank my parents, and my family for their encouragement and constant support.

My thanks and appreciations also go to my colleagues Adam, Johnathan, and Toky for the advice and support.

Table of Contents

Table of Figures

Table of Tables

List of Acronym

FPGA:	field programmable gate arrays
AVMD:	adaptive variational mode decomposition
IMF:	intrinsic mode function
DAQ:	data acquisition
ADC:	analog-to-digital converter
MCU:	microcontroller unit
SAR:	successive approximation register
FT:	Fourier transfer
RMS:	root-mean-square
WVD:	Wigner-Ville distribution
WT:	wavelet transform
HHT:	Hilbert-Huang transform
EMD:	empirical mode decomposition
LUT:	lookup table
CORDIC:	coordinate rotation digital computer
RT:	recursive trigonometric
DAC:	digital-to-analog converter
CLBs:	configurable logic blocks
API:	application programming interface
I/O:	input/output
RAM:	random-access memory
PLLs:	phase-locked loops
Op-Amp:	operational amplifier
IEPE:	integrated electronics piezo-electric
MOSFET:	metal–oxide–semiconductor field-effect transistor
GOIO:	general-purpose input/output
FFT:	fast Fourier transform
THT:	Teager-Huang transform
CWRU:	case western reserve university

Chapter 1

Introduction

1.1 Background

Rotating machines are commonly used in almost every aspect of people's daily lives such as vehicles, motors, turbines, and robots. Failures of a rotating machine may result in reduced production quality, degraded safety, increased costs in repairs and maintenance, or even potential risk of loss of life [1]. Rolling element bearings, which are referred to as bearings thereafter, are essential components in rotating machinery to support rotating shafts and reduce frictions. Based on investigation [2], up to 75% of imperfections in small- and medium-size rotating machines, and 50% of imperfections in large-size machines, are related to bearing faults. Therefore, a reliable and effective bearing fault detection technology is critically needed in industries to identify a bearing defect at its earliest stage so as to improve machinery performance, increase productivity, and reduce maintenance costs.

Before introducing the bearing fault, it is important to understand bearing structure. Depending on the shape of the rolling element, rolling element bearings can be classified as ball, tapered, cylinder, and needle bearings. Figure 1.1 shows a typical ball bearing structure, which consists of an outer ring, an inner ring, a set of rolling elements (balls), a bearing cage, and a bearing seal.

Figure 1.1: Rolling element bearing structure: (1) outer ring, (2) inner ring, (3) cage, (4) rolling element, and (5) bearing seal [3].

Typically, bearing defects can be classified as "distributed" and "localized" defects [4]. Distributed defects are usually caused by excessive misalignment errors, improper mounting,

and abrasive wear, which can result in bearing surface roughness, waviness, misaligned raceways, etc. [5]. Localized bearing faults usually are associated with fatigue damage caused by the dynamic stress during operation [4]. This work will focus on localized bearing fault detection, which is more important from maintenance perspective.

Bearing fault detection can be performed by analyzing different types of information carriers, such as acoustics, electric current, lubricant, thermal, strain, and vibration [6]. Vibration signals have a relatively high signal-to-noise ratio and are easy to measure [7], which are most commonly used for bearing health monitoring. This research will also be based on the analysis of vibration signals.

To collect these vibration signals, a high-speed and high-resolution data acquisition (DAQ) system is indispensable. The role of the DAQ system is to convert the vibration analog signals to digital signals and then transfer to a computing device (usually a PC) for processing. The terminal software in the computer will use the relevant signal processing techniques to extract representative information to diagnose the fault of the bearing of interest.

1.2 Data Acquisition (DAQ) Systems

A DAQ system measures a physical phenomenon (e.g., vibration, current, temperature, pressure, or sound) [8], preprocesses the data, and transmits the signals to a computer for analysis. In addition, a modern DAQ system should provide real-time and post-recording functions for data visualization and primary analysis [9]. A smart DAQ system mainly consists of four essential units that form the entire measurement chain of physics phenomena: a sensing unit, signal conditioning, analog-to-digital converter (ADC), and a microcontroller unit (MCU) to control the processes. Figure 1.2 illustrates the functional units of a typical smart DAQ system.

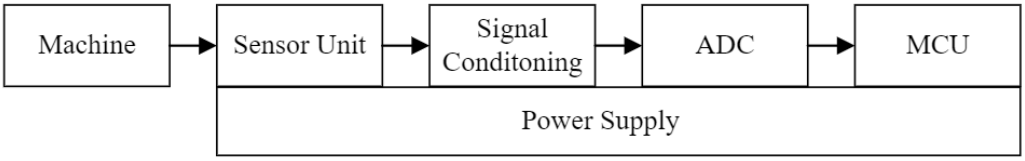

Figure 1.2: A block diagram of a smart DAQ system.

The sensing unit measures a physical quantity (e.g., mechanical, chemical, radiant, and thermal) and transforms it to an electrical signal [10]. In this case, the physical signal is

related to mechanical vibration. The measurable analog electrical quantities could be in terms of voltage, current or charge for further display or processing [8].

Signal conditioning in a DAQ system is to provide the essential functions for accurate measurements, including electrical isolation, amplification, signal filtering, offset adjustment, compliance with sensor requirements, etc. [11]. Electrical isolation is the separation of the circuit from other sources of electromotive force. In general, the signal magnitude from the sensing unit is relatively weak, which should be amplified in magnitude. Adding electrical isolation can avoid the previous situation and reduce noise generated by electrical potential. Signal amplification is a process of amplifying signals for processing or visualization. There are different types of amplifiers used for different purposes in signal conditioning. Signal amplification can be done by increasing the resolution/amplitude of the input signal or by increasing the signal-to-noise ratio. In short, the signal amplification is incorporated in the signal conditioning circuit, which can better capture the valid information from the measured signal.

Filtering is a processing function in which some signal frequency components are filtered out on request. There are several types of filters, such as low-pass, high-pass, band-pass, and band-stop filters. Filters can also be made from passive or active components and in analog and digital forms. For example, passive filters are composed of passive components such as resistors, capacitors, and inductors. There are no amplifying elements (transistors, operational amplifiers, etc.), so there is no signal gain, and their output level is always smaller than the input. In contrast, active filters use active components, such as operational amplifiers, in addition to resistors and capacitors, but do not use inductors. Active filters are capable of handling very low frequencies (close to 0 Hz), and they can provide voltage gain to the output signal. Unlike passive and active analog filters, a digital filter is a software system that performs mathematical operations on a sampled discrete-time signal to reduce or enhance some aspect of that signal [12]. Therefore, selecting the appropriate filtering method is very important for the signal quality of DAQ.

An analog-to-digital converter (ADC) can be a crucial part of a DAQ system to convert the measured analog signal to a digital (discrete) counterpart for advanced processing. Successive approximation register (SAR) and Delta-Sigma are common types of ADC structures in modern DAQ applications. SAR ADC can provide up to 18-bit resolution and sampling rates up to 1 MHz. Although SAR does not have inherent anti-aliasing protection, it is still commonly used in ADCs due to its balanced performance and low cost. Compared to

SAR, Delta-Sigma ADCs are more expensive but have higher dynamic performance and inherent anti-aliasing protection, which has a resolution of up to 32 bits and a maximum sampling rate of 1 MHz [13].

DAQ software offers the necessary visualization, analysis, and control functions within a DAQ system. The data storage strategy depends on the application requirements. In the DAQ system, signals are periodically acquired with a required sample size, and then the data is transferred to a computing device or the cloud [14, 15]. Nowadays, flexible DAQ systems allow users to visualize and examine data in real-time during measurement procedures and configure the display using built-in graphical components with standard signal processing techniques, such as the Fourier Transfer (FT), signal average, and spectrum analysis.

The traditional wired DAQ systems have been commonly used in industrial applications [16]. A wired DAQ system has the characteristics of stability and accuracy. Usually, it uses a cable to connect the DAQ to the computer or the portable tablet. Figure 1.3 shows an example of a wired based DAQ system from National Instrument. This wired connection mode can provide the feasibility of high-speed data transfer from the microcontroller unit (MCU). However, in actual use, the installation and maintenance costs of wired DAQ systems are usually high and the signal resolutions are limited due to performance of MCU.

Figure 1.3: A typical wired DAQ system from National Instrument [17].

A wireless DAQ system contains the main body of the wired DAQ system, but the difference is to transmit the acquired digital signal wirelessly to the computing device. The common wireless communication protocols include RF, ZigBee, and Wi-Fi, among others. Considering the previous work in our research group, Sengoz proposed a 6.5 kHz sampling

rate, RF-based wireless DAQ system [18]. Due to the limitation of the ADC chip operating frequency, its sampling rate is not fast enough to qualify different bearing conditions. Cheng proposed a 24-bit resolution, ZigBee wireless DAQ system [19]. In real applications, the signal could be lost sometimes due to obstacle blockage. Based on Cheng's work, Toky designed a Wi-Fi wireless DAQ system [20]. However, its high-speed ADC sampling rate leads to data buildup thus disguising the ADC transmission rate. As a result, the wireless DAQ systems also exist some drawbacks and problems. Therefore, combining the advantages of wired DAQ and wireless DAQ will be the guideline to design a new DAQ system in this work. In addition, to explore new DAQ design ideas using the FPGA is worth to be considered. Furthermore, other challenges of the new DAQ system will also be related to the high-speed sampling rate and robust transmission approach.

1.3 Bearing Fault Detection

Figure 1.4 illustrates a typical example of a rolling element bearing with a rotating inner race and a fixed outer race. A localized fatigue defect is in the outer race of the bearing. In the bearing structure, the load on the shaft is transferred through the load zone to the inner ring, the rolling element, and then the outer ring. In operation, the rolling elements will pass through the load zone in sequence based on a certain period. This repetitive loading generates high pressure on the raceway surfaces of the inner race and outer ring in contact with the rolling surface of the rolling elements. Consequently, material fatigue pitting can occur as shown in Figure 1.4 on the surface of a bearing component (the outer race in this example) due to fatigue caused by repeated contact stress.

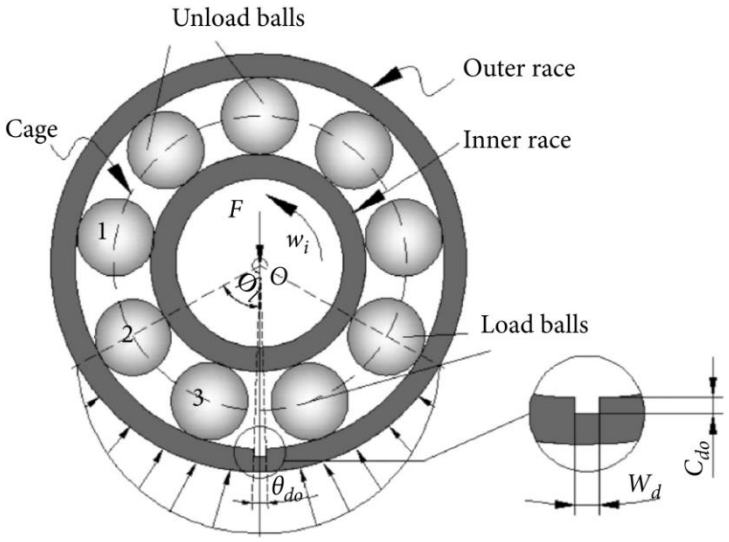

Figure 1.4: A rolling element bearing load zone distribution with an outer race fatigue pit [21].

In addition, as the rolling elements pass through the load zone in sequence based on a certain period, the specific vibration frequencies and noise will be generated by the dynamic changes as the bearing rotates. Vibration is also generated even if the bearing is healthy. When a bearing element is damaged, impulses are generated whenever defects on the bearing interact with the bearing element. These impulses will excite the natural frequencies of the bearing system and housing structure, increasing the vibration energy of the bearing elements at specific frequencies [6]. Fault detection is to recognize these fault-related representative features to predict bearing defects [22].

Based on the bearing dynamics analysis, the characteristic frequency of bearing faults can be calculated [23]. Consider a ball bearing shown in Figure 1.5, which has pure rolling contact, sound installation, and stable operating conditions. The related parameters of this ball bearing include the ball diameter d, the pitch diameter D, the contact angle θ, and the total number of rolling elements Z. If the speed of the rotating inner ring is n rpm, or $f_r = n/60$ Hz, different characteristic frequencies of bearing faults can be calculated in following procedures:

The characteristic frequency for the bearing outer race defect is

$$f_{od} = \frac{Zf_r}{2}\left(1 - \frac{d}{D}\cos(\theta)\right) \text{ (Hz)} \tag{1.1}$$

The characteristic frequency for the bearing inner race defect is

$$f_{id} = \frac{Zf_r}{2}\left(1 + \frac{d}{D}\cos(\theta)\right) \text{ (Hz)} \tag{1.2}$$

The characteristic frequency for the bearing rolling element defect is

$$f_{ed} = \frac{Df_r}{2}\left(1 - \frac{d^2}{D^2}\cos^2(\theta)\right) \text{ (Hz)} \tag{1.3}$$

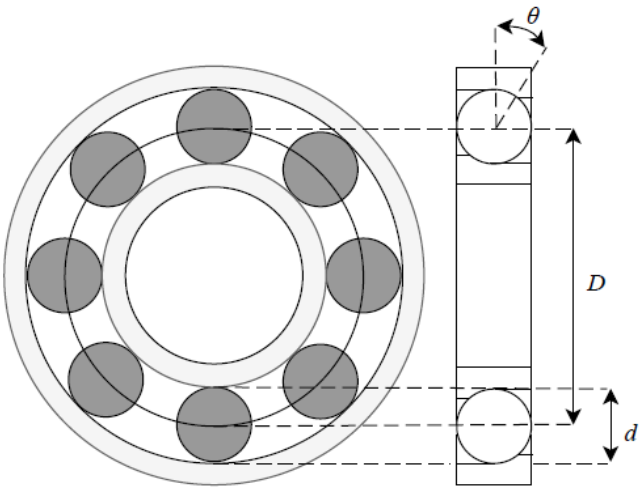

Figure 1.5: kinematics structure of a ball bearing [18].

1.4 Signal Processing Techniques for Bearing Fault Detection

After the vibration signals are collected by using a DAQ system, bearing representative features can be extracted by using appropriate signal processing techniques. There are many signal processing techniques in literature for bearing fault detection, which can be classified as analysis in the time domain, frequency domain, and time-frequency domain. In time domain analysis, the main principle of bearing fault detection is based on analyzing the statistical parameters of the signal, such as peak value, peak-to-peak value, root-mean-square (RMS), crest factor [24], skewness, kurtosis [25], spectral kurtosis [26], impulse factor, shape factor, and clearance factor [27]. In general, signals can be roughly divided into stationary and non-stationary. The advantages of time domain analysis for stationary signals are its simplicity in computation and fast processing speed. However, most fault-related features are non-stationary, and then time-domain analysis lacks the accuracy and sensitivity for bearing fault detection. Therefore, it is necessary to introduce the frequency domain and time-frequency domain analysis for bearing fault detection.

Frequency domain analysis is to transform the time signal to the frequency domain representation for analysis by using different forms of the FT [28, 29]. Each bearing component has a specific characteristic frequency calculated using Eq. (1.1)-(1.3). Bearing fault detection is undertaken to examine the resulting spectral maps with respect to these theoretical fault characteristics. However, in actual fault analysis, the signal is often mixed with noise and some defect-related features are time varying (e.g., rolling element defect), which makes it difficult to identify the fault frequency components on spectral maps. The

methods, including power spectrum [30], cestrum spectrum, and Hilbert demodulation [31], are proposed to reduce the noise and improve the signal-to-noise ratio. Nevertheless, the generality of these methods is limited, and the accuracy still depends on the defect location, bearing dynamics, and rotation speed.

Time-frequency analysis has been widely used to analyze non-stationary signals. Time-frequency analysis can compose the complex structure of signals that contain multiple components and provide direct information about the frequency components occurring at any given time [30]. Common time-frequency analysis methods include the short-time FT [31], Wigner-Ville distribution (WVD) [32], wavelet transform (WT) [33], wavelet packet analysis, Hilbert-Huang transform (HHT) [34], etc. However, each method has its own advantages and limitations in the practical processing applications. For example, the short-time FT may not be able to provide valid information including simultaneous time and frequency localization at the same time. Besides, applying WVD and other bilinear time-frequency distributions in bearing fault detection is limited due to the potential cross-interference items [35]. Moreover, the WT is inefficient for processing signals whose energy is not well concentrated in the frequency domain [36]. On the other hand, in HHT analysis, empirical mode decomposition (EMD) is a self-adaptive method for non-stationary signal analysis [37]. However, it has limitations in mode mixing, over envelope, or less envelope, which will affect the processing accuracy [38]. Therefore, it is still remaining a challenging task to extract robust representative features from non-stationary vibration signals for bearing fault detection, especially when defect occurs on the rotating ring and rolling elements. This work aims to provide a new signal processing technique to improve the reliability for bearing fault diagnosis.

1.5 Research Objectives

The overall research objective of this work is to continue the previous development projects in our research group and develop an online monitoring system for real-time bearing fault detection. It consists of two topics:

The first objective is to develop a high-speed sampling and high-resolution DAQ system to collect vibration signals.

The second objective is to propose an adaptive Variational Mode Decomposition (AVMD) technique for non-stationary signal analysis and bearing fault detection. The effectiveness of

the proposed AVMD technique is examined by experimental tests corresponding to different bearing conditions. Its robustness in bearing fault detection is examined using the data sets from a different experimental setup.

1.6 Thesis Outline

The remaining chapters in the thesis are organized as follows:

Chapter 2 discusses the development of an FPGA sinusoidal waveform generator and explores its potential application in DAQ systems.

Chapter 3 describes the development of the DAQ system.

Chapter 4 discusses the proposed AVMD technique for bearing fault detection.

Chapter 5 describes the simulation and experimental tests to examine the effectiveness of the proposed AVMD technique under different bearing testing conditions.

Chapter 6 summarizes concluding remarks from the research activity in this work and identifies further research to advance the technical knowledge in this field.

Chapter 2

Development of A FPGA Sinusoidal Waveform Generator

In modern electronic systems, a sinusoidal waveform can be a comparator, a tracker, or a simulation source, which can be used in interstellar communication, satellite communication, 5G mobile communication, system control, digital signal processing, etc. [39, 40]. Several embedded platforms such as the field programmable gate array (FPGA), microcontroller unit (MCU) and application-specified integrated circuitry can help implement trigonometric functions in electronic systems [41]. The lookup table (LUT) [41], polynomial approximation [42], and coordinate rotation digital computer (CORDIC) [43-46] are the main algorithms for implementing the trigonometric functions in these embedded platforms.

This chapter aims to develop a new sinusoidal waveform generator in the FPGA and explore its possible applications for high speed DAQ applications.

2.1 Principle of Recursive Trigonometric (RT) Algorithm

The proposed RT technique is based on the trigonometric identities to conduct trigonometric function calculation. The cosine functions can be calculated easily using other trigonometric functions (e.g., sine, tangent, and cotangent) and be transferred by the trigonometric identities. Once the value of cosine is calculated, the sine value can be easily obtained by phase transformation. Eq. (2.1) and Eq. (2.2) are the basic cosine and sine functions and expansions:

$$\cos\big((n+1)\theta\big) = \cos(\theta)\cos(n\theta) - \sin(n\theta)\sin(\theta) \tag{2.1}$$

$$\sin(n\theta)\sin(\theta) = \frac{1}{2}[\cos(n\theta-\theta) - \cos(n\theta+\theta)] \tag{2.2}$$

Based on the trigonometric identities in Eq. (2.1)-(2.2), the following representation can be obtained:

$$\cos\big((n+1)\theta\big) = \cos(\theta)\cos(n\theta) - \frac{1}{2}[\cos(n\theta-\theta) - \cos(n\theta+\theta)] \tag{2.3}$$

Eq. (2.3) can be simplified as:

$$\cos\big((n+1)\theta\big) = 2\cos(n\theta)\cos(\theta) - \cos\big((n-1)\theta\big) \tag{2.4}$$

The RT technique will be derived from the trigonometric identities transform in Eq. (2.4), specifically:

If $n = 1$,

$$\cos(2\theta) = 2\cos(\theta)\cos(\theta) - \cos(0) \tag{2.5}$$

If $n = 2$,

$$\cos(3\theta) = 2\cos(2\theta)\cos(\theta) - \cos(\theta) \tag{2.6}$$

……

If $n = k$,

$$\cos(k\theta) = 2\cos\big((k-1)\theta\big)\cos(\theta) - \cos\big((k-2)\theta\big) \tag{2.7}$$

From Eq. (2.5) to Eq. (2.7), it can be seen that given an initial angle θ, we can calculate the values of $\cos(\theta)$ and $\cos(2\theta)$ using Eq. (2.5). This process can be repeated recursively to compute cosine values of $\cos(k\theta)$, where k is an integer. Therefore, once the initial θ is selected, all cosine values of $\cos(k\theta)$ can be computed, where $k\theta \in [0, 2\pi]$.

2.2 FPGA

The hardware of the sinusoidal waveform generator consists of two main parts. The first part is FPGA, which is the core of the system and is responsible for running the algorithms and generating the digital signals, which will be discussed in this section. The second part is the digital-to-analog converter (DAC), which will be discussed in section 2.3.

2.2.1 FPGA Overview

FPGA is defined as a matrix of configurable logic blocks (CLBs) (combined and/or sequential) with user-programmable interconnects, tailored to operate for specific applications [47]. Unlike conventional processors, FPGA executes operations in a parallel mode, as shown in Figure 2.1, so that different processing operations do not have to compete

for the same resources. For CPU operation structure shown in Figure 2.1, it is structured to run in a top-down sequence, which means the software comments need to transfer through drive application programming interface (API) to the operating system and then to the hardware. This operation structure of the CPU will take longer response times and slower program operation. In contrast, for FPGA, each independent processing task is assigned to a dedicated part of the chip and can run autonomously, without any influence from other logic blocks. Therefore, when adding more instructions to execute, the performance of one part of the application will not be affected.

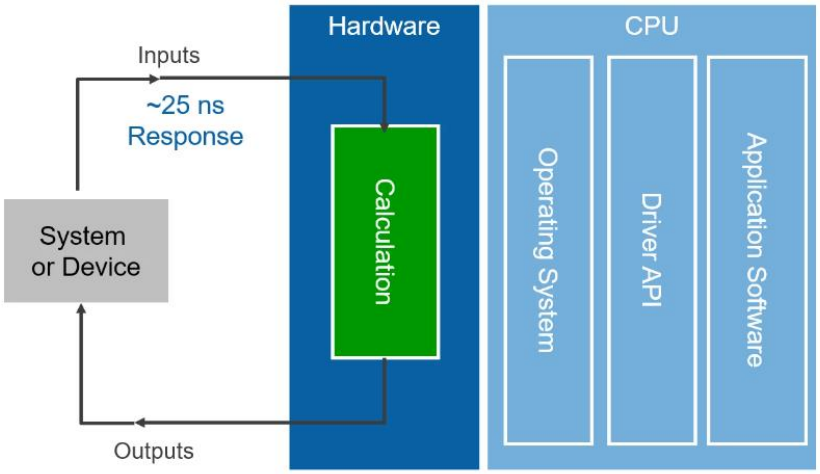

Figure 2.1: FPGA processing structure [48].

Figure 2.2 shows the FPGA generic architecture; it is composed of a matrix of CLBs, surrounded by a system of programmable interconnects, which routes signals between CLBs. Input/output (I/O) blocks interface the FPGA with external devices.

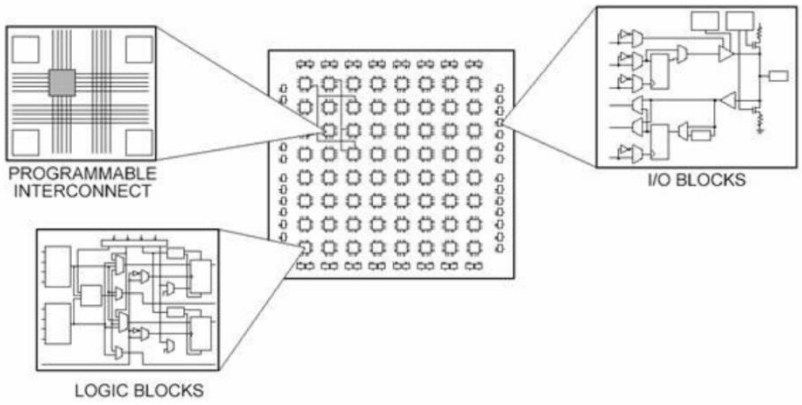

Figure 2.2: Generic architecture of an FPGA [48].

The CLBs are the basic logic unit of an FPGA. Depending on the manufacturer, the CLB may also be referred to as a logic block, a logic element, or a logic cell [48]. The CLB consists of two basic components: a flip-flop and a LUT [49], as illustrated in Figure 2.3. The flip-flops are binary shift registers used to synchronize the logic and keep the logic state between clock cycles of the FPGA circuit. At each clock edge, a flip-flop latches a value of 1 or 0 (i.e., true or false) on its input and holds that value until the next clock edge. For the LUT, most of the logic in the CLB is implemented as a LUT with a very small amount of random-access memory (RAM). All combinational logic (AND, OR, NAND, XOR, etc.) is implemented in LUT memory in the form of truth tables. The truth table is a predefined list of outputs for each input combination [47].

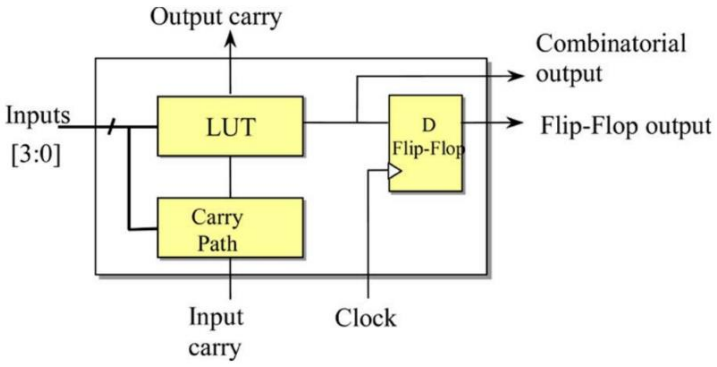

Figure 2.3: A structure of configurable logic blocks [48].

There are many FPGA options from different manufacturers such as Xilinx, Inc., Intel Corporation, Microchip Technology Inc., Lattice Semiconductor Corporation, and QuickLogic Corporation [50]. The FPGA selected for this development work is from Cyclone IV E family FPGA (EP4CE15F23C8 from Intel) with low power consumption, relatively high performance, and available development tools. As shown in Figure 2.4, EP4CE15F23C8 is an FPGA with 15000 CLBs, 4 I/O Phase-Locked Loops (PLLs), and 504 Kb Embedded Memory.

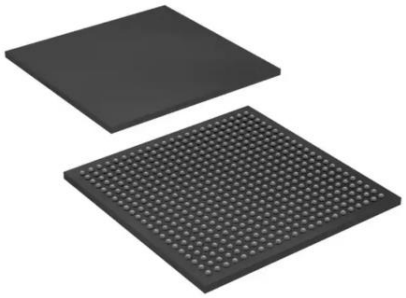

Figure 2.4: FPGA of EP4CE15F23C8 [51].

2.2.2 FPGA Architectures of the RT Technique

In the proposed RT technique, the trigonometric calculation will cover each cosine value between 0 to 2π. If the initial angle is 0 rad, when $n = 1$, the initial input will be $\cos((1-1)\theta) = \cos(0)$. In addition, the iteration step size of the angle should be appropriately selected so that the following input will be the cosine value of this step size angle.

The iteration step can be an integer angle, a fractional angle, in radian or degree; but the angle should be an integer multiple of 2π or 360 degrees. Figure 2.5 shows the digital architecture to keep those two cosine values in the RAM. The shifter will shift the step size angle to the left or multiply by 2. The result becomes $2\cos(\theta)$, which will be multiplied by $\cos(n\theta)$ according to Eq. (2.5). Then, $2\cos(\theta)\cos(n\theta)$ will be subtracted by $\cos((n-1)\theta)$ in the accumulator, which results in $2\cos(\theta)$ and is stored in the RAM for the following calculations. The RT technique contains only one clock cycle multiplication, addition, and subtraction; its accuracy depends on the initial value of $\cos(\theta)$, which can be controlled by certain bits of devices or systems.

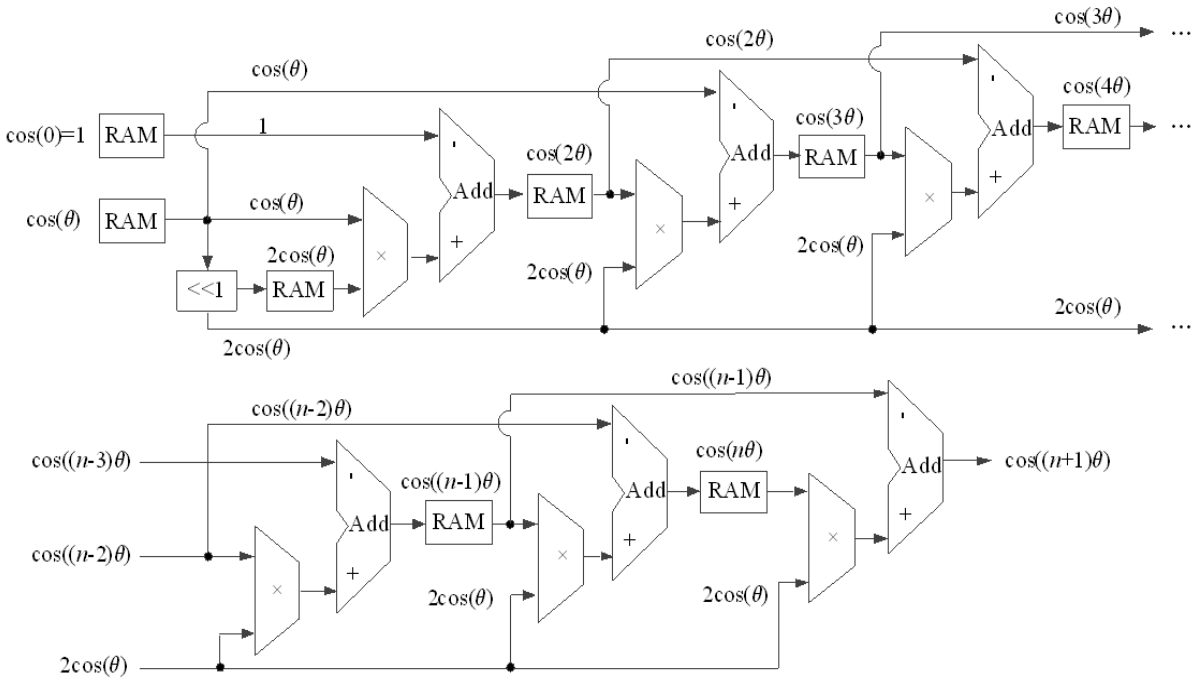

Figure 2.5: The architecture of the RT algorithm.

2.3 Digital to Analog Converter (DAC)

The DAC, as the second part of the sinusoidal waveform generator, has the main function of converting the digital signal generated by the FPGA into an analog signal. In this development, AD9709 chip (from Analog Device Inc.) is selected as the DAC component, which has the following features [52]:

1) 175 million of samples per second (MSPS) update rate;
2) Low power dissipation (12mW at 80 MSPS, 50mW at 175 MSPS);
3) Two channels with 8 bits resolution output;
4) Wide supply voltage: 1.7 V to 3.6 V;
5) Self-calibration.

Both channels of the AD9709 support voltage outputs from 0.48 to 2.2 V. The relationship between the output voltage and the input data can be expressed by:

$$V_{out} = -1.72 \times (D_{AC\_DA} / 255) + 2.2 \tag{2.8}$$

where factor "-1.72" is the constant based on the datasheet [52]; D_{AC_DA} is the register value

from algorithm calculation results; “255” is a resolution divider due to the 8-bits resolution of the AD9707; “2.2” is a reference voltage supplied by FPGA.

It should be noted that the output voltage in the specific range from 0.48V to 2.2V is related to the developed circuit only, which may be different in other circuits.

2.4 Simulation Testing

Some simulations will be undertaken in this section to use the proposed RT technique to generate some cosine waveforms. The RT technique will be implemented in MATLAB. The RT effectiveness will be examined by comparing its performance with the related methods under the same frequency and bandwidth. In addition, for the convenience of comparison with other related algorithms, all computed results are in cosine values.

Figure 2.6 shows simulated cosine waveforms in MATLAB, using the RT technique. The step angle is 0.063 rad used for both RT and CORDIC method, where CORDIC uses the same setting as in paper [53]; the scale factor $K = 0.607$ is used for radix-2 CORDIC with 16 iterations. The scale factor K is a variable for radix-4 CORDIC, with 8 iterations [54]. For the RT technique, the initial value is the cosine value of step angle and cos(0) = 1 is used to complete the first recursive calculation. The step angle and cos(0) are used to compute the following cosine values recursively using Eq. (2.5). The result precision will be kept in 16 bits, which will be used for computation of each algorithm.

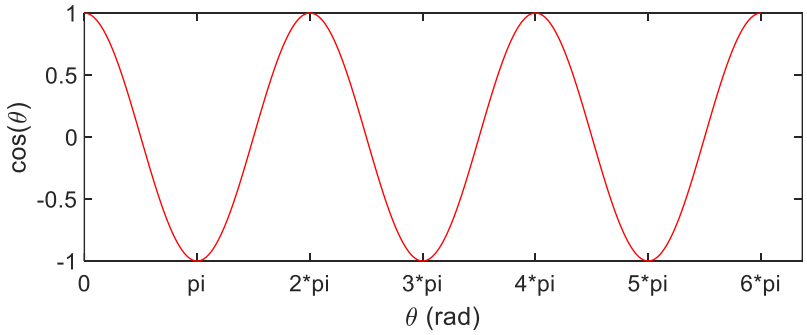

Figure 2.6: The RT cosine waveform simulation by MATLAB.

The MATLAB function “cos” will be used to calculate the reference value to compare the accuracy of the RT, Radix-2, and Radix-4 CORDIC. The 16-bits comparison of these three

methods with reference value is shown in Figure 2.7.

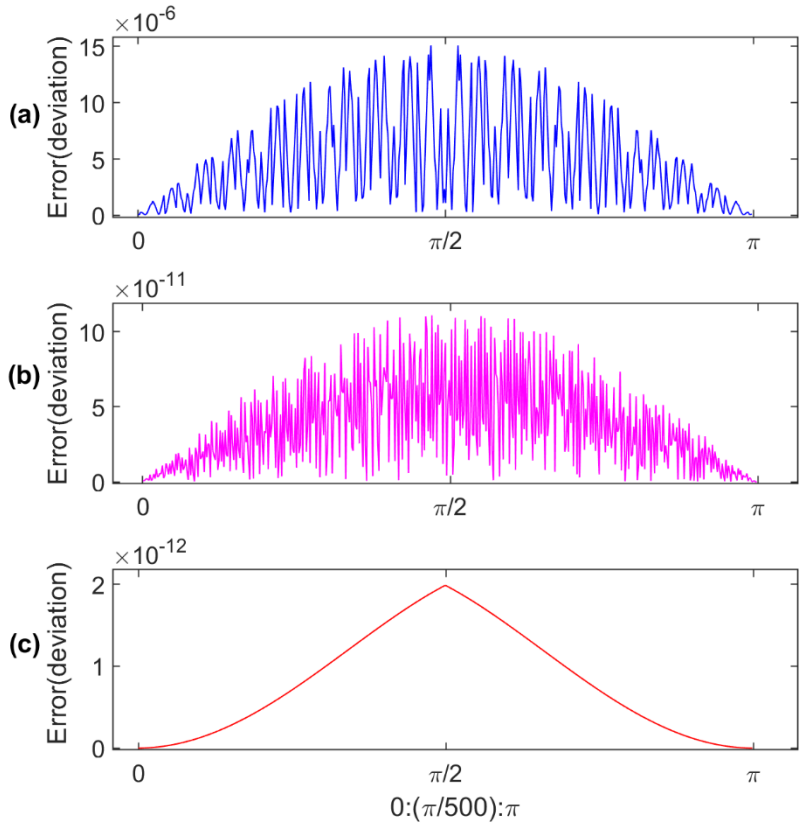

Figure 2.7: 16-bits accuracy comparison between different methods: (a) Radix-2, (b) Radix-4, (c) RT.

As demonstrated in Figure 2.7, the maximum CORDIC difference error occurs around $\pi/2$. For the Radix-2, the maximum error is 1.590×10^{-5}; for the Radix-4, the maximum error is 1.109×10^{-10}. For the proposed RT technique, the maximum error is 1.983×10^{-12}. For RT technique, the processing errors mainly come from two aspects: 1) the pre-define cosine value; 2) the accumulated truncation errors in the recursive calculation. The former error can be reduced by using more accurate input cosine value such as 24 bits or 32 bits in binary format. The latter error can be tackled by using quadrant transformation. The angle domain is [0, $\pi/2$] and the angle over $\pi/2$ can be transformed to [0, $\pi/2$]. For example, the value of $\cos(3\pi/2)$ can be transformed to $\cos(\pi/2)$. As shown the in Figure 2.7(c), the errors are reduced between $\pi/2$ and π by the quadrant transformation. For the CORDIC method, because the CORDIC has angles only over [-1.74, +1.74] rad or [-99.99, +99.99] deg, based on $\tan(\theta)$, it can calculate two quadrant angles only, and the angle out of this interval will be converted into [-1.74, +1.74] rad or [-99.99, +99.99] deg. As a result, the computational

error increases as the number of iterations increases. In addition, the scale factor *K* affects the accuracy of CORDIC. The Radix-2 CORDIC is an approximate calculation algorithm, and its final cosine value needs to be multiplied by a scale factor of approximately 0.6073 as the number of iterations reaches infinity. For the Radix-4 CORDIC, the scale factor *K* is not a constant [54] but is calculated by

$$K = \prod_i (1 + \sigma_i^2 \times 4^{-2i})^{\frac{1}{2}} \tag{2.9}$$

where σ_i belongs to a digit set $\{-a, \dots, 0, \dots, +a\}, a \in [2, 3]$. i is the number of iterations, when i achieves n bits its precision is $n/2$. σ_i can be determined by an angle interval. Different angles in each iteration will result in a different σ_i value. Although Radix-4 CORDIC can decrease the iteration operation times, its scale factor calculation is more complex compared with Radix-2 using Eq. (2.9).

To further examine the effectiveness of the proposed RT technique in calculation accuracy, some comparison tests are undertaken in terms of the root mean square error (RMSE). Table 2.1 summarizes results of different algorithms to generate cosine waveforms and relative RMSE under 16-bits and 32-bits, respectively. CORDIC II [55] is the improved CORDIC algorithm that reduces the number of iterations by classifying the iteration angles. Hybrid CORDIC [53] is a CORIDC that adds a double iteration based on the Radix-4 CORDI. However, the CORDIC or its extended methods such as Hybrid CORDIC and CORDIC II are approximation algorithms; their cosine values depend on not only the iterations but also the accuracy of the scale factor *K*. On the other hand, it is seen from Figure 2.7 and Table 2.1 that the proposed RT technique outperforms the other related algorithms in precision. Different to CORDIC, the RT algorithm calculates the input mathematically based on Eq. (2.4). The result is an exact value from the input, and its accuracy will not be lost in the calculation process.

Table 2.1: Comparison of different algorithms to generate cosine waveforms.

Algorithm	16-bit cosine EMSE	32-bit cosine EMSE
Radix-2	1.39×10^{-4}	1.69×10^{-6}
Radix-4	6.85×10^{-5}	1.07×10^{-6}
CORDIC II	8.70×10^{-3}	N/A
Hybrid	1.70×10^{-5}	N/A
RT	2.82×10^{-9}	1.02×10^{-12}

2.5 FPGA Implementation of the Sinusoidal Waveform

To further verify the effectiveness of the proposed RT technique, more tests are undertaken using the experimental setup as shown in Figure 2.8. The RT technique is coded in Verilog [56], synthesized using Quartus software [57], and implemented on the Cyclone IV E FPGA (EP4CE15F23C8 from Intel). The digital output is converted to an analog signal by a DAC unit (AD9707 from Analog Device Inc). The input is 32-bits binary format. The outputs from the DAC are scaled such that the first and second bits are used for the plus/minus sign bit and decimal point bit, respectively. Figure 2.9 shows the sinusoidal waveform using the RT technique.

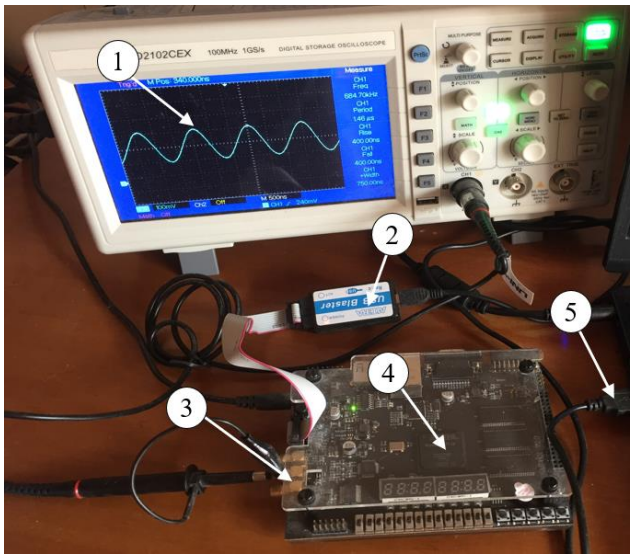

Figure 2.8: Experiment Setting of FPGA implementation of the cosine waveform: (1) Oscilloscope; (2) FPGA USB blaster; (3) DAC output; (4) Cyclone IV E FPGA; (5) PC.

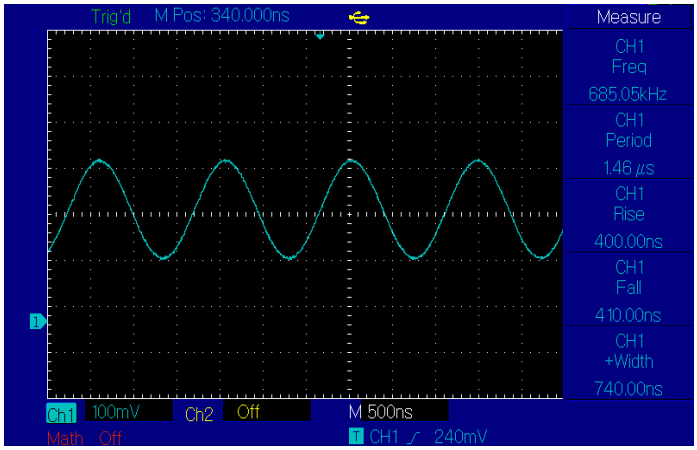

Figure 2.9: Cosine waveform generated by Cyclone IV FPGA using the RT technique.

The initial angle is 0.086 rad so a complete sinusoidal cycle requires the generation of 73 sine values. Considering that the input clock of the FPGA I/O pins is 50 MHz, which is equivalent to a period of 20ns, the cycle frequency of the final DAC output is calculated by

$$f_{OUT} = \frac{1}{73 \times 20 \times 10^{-9}} = 684931 \quad \text{(Hz)} \tag{2.10}$$

which has a similar result shown in the Figure 2.9. The actual experimental results are fully consistent with the theoretical calculations and verify the effectiveness of the RT technique.

It would be stated that although the RT algorithm has demonstrated its superior performance in the Cyclone IV E FPGA, it would not be used as the processor unit for the DAQ system in this study. The selected ADC requires an SPI interface for data transfer; however the Cyclone IV E FPGA does not have this interface in the peripheral. In addition, the related supplementary chips could not be purchased due to the breakout of supply chains. However, when the related chips are available later, the FPGA processing technology would be used in the future generation of the wireless DAQ system used in the Bare Point Water Treatment Plant in Thunder Bay, Ontario.

2.6 Summary

In this chapter, a new RT technique has been proposed for FPGA implementation of the sinusoidal waveform. The model of RT technique is constructed based on the trigonometric identities. The accuracy of the RT technique is verified by comparing it with other related methods by simulation tests. The feasibility of the RT technique is verified in FPGA

experiment, which is important to improve FPGA functionality and performance, as well as the subsequent design of the FPGA-based DAQ system.

Chapter 3

Development of a DAQ System Prototype

In this chapter, a DAQ prototype will be developed to meet specific requirements for bearing fault detection, which include integrated electronics piezo-electric (IEPE) support, high-speed, high resolution, and reliable data transmission. The detail of design will be introduced in following section and the system verification will be demonstrated on this chapter as well. It should be stated that due to the supply chain breakdown caused by the COVID pandemic, several designed electronic chips could not be available in the market. Correspondingly, a wired DAQ system prototype is develop in this work without using the FPGA and wireless communication.

3.1 Sensing Unit

As discussed in Chapter 1, in this work, vibration signals will be used for analysis and predict bearing health conditions. The characteristic frequencies of the vibration signal will be used as the basis for fault diagnosis. The IEPE vibration sensors will be selected as the sensing units in this research.

The IEPE vibration sensor chose for this research is 603C01 (from IMI Sensors). It is a shear-design sensor, as shown in Figure 3.1. The merits of shear-design sensors are inherent in sensitivity to adverse environmental influences, such as case or base strain and thermal transients [58]. In addition, its internal case isolation and shielding are essential in avoiding erroneous signals resulting from ground loops and pick-up of electromagnetic and radio frequency interference. Its other unique properties include non-magnetic stainless-steel housing, hermetic sealing, and industrial-military connectors.

The output parameters and usage requirements of the 603C01 [58] are listed in Table 3.1. The details of the power supply designed according to the application requirements will be discussed in the next subsection.

Table 3.1: 603C01 Sensor performance and characteristics [58].

Parameter	Specification
Sensitivity	100mV/g
Measurement range	±50g
Frequency measurement range	0.5 Hz to 10kHz
Temperature range	-54 to +121°C
Sensor excitation voltage	18-28V
Sensor excitation current	2-20mA
Output bias voltage	8-12V

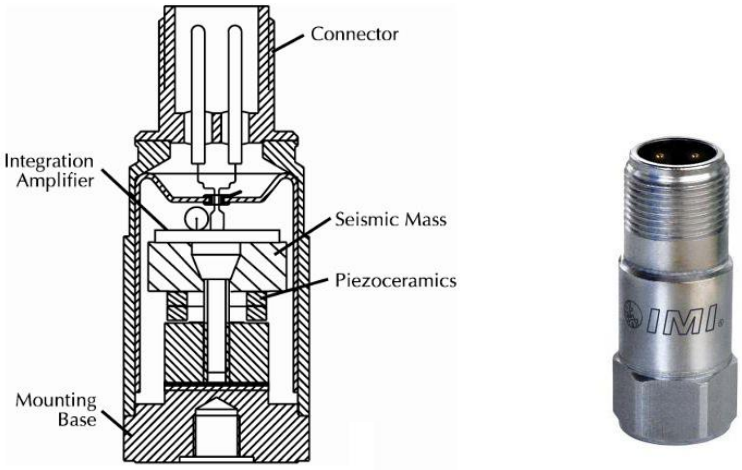

(a) (b)

Figure 3.1: (a) Illustration of a typical shear mode accelerometer [59] (b) A 603C01 sensor [58].

3.2 Sensor Power System

Based on the power requirements of the sensing unit as discussed in the previous section, an appropriate power circuit will be designed in this section. The design of the power supply circuit will be divided into two parts: the voltage design and the constant current source design. The specific design processes are discussed next.

3.2.1 Excitation Voltage Circuit Design

Since 603C01 is an active IEPE accelerometer, it requires an external excitation voltage source ranging from 18V to 28V; 24V is selected in this project, which is chosen by the

available laboratory equipment and practical experience. Due to limitations in application environment, a 9V battery (from Duracell) [60] will be used as the primary power source in this project. A boost converter circuit will be designed to reach the required excitation voltage of 24V. To obtain 24V voltage, MC34063a (from Texas Instrument) is used to construct the boost converter circuit as shown in Figure 3.2.

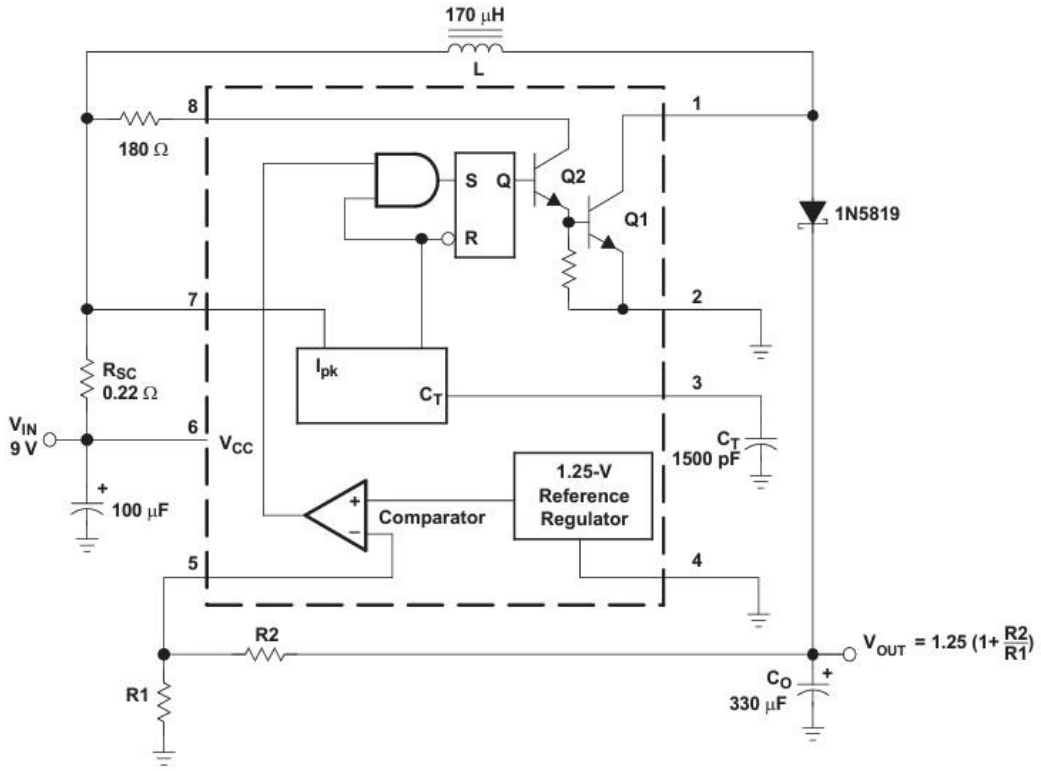

Figure 3.2: The structure of the boost converter circuit [61].

The output of the circuit depends on the value of R_1 and R_2 will be [61]:

$$V_{OUT} = 1.25\left(1+\frac{R_2}{R_1}\right) \tag{3.1}$$

In this case, the output voltage is V_{OUT} = 24V. Therefore, the ratio of R_1 and R_2 can be determined by:

$$\frac{R_2}{R_1} = \frac{V_{OUT}}{1.25} - 1 = \frac{24}{1.25} - 1 = 18.2 \tag{3.2}$$

If R_1 is selected as 3kΩ, the value of R_2 will be selected as:

$$R_2 = R_1 \times 18.2 = 3 \times 18.2 = 54.6 \quad (\text{k}\Omega) \tag{3.3}$$

Since there is no 54.6kΩ resistor available in our lab, we use a 51kΩ and a 4.7kΩ resistor to make a series connection, which results in R_2 = 55.7kΩ. Then the updated theoretical output value V_{OUT} will be:

$$V_{OUT(updated)} = 1.25\left(1+\frac{R_2}{R_1}\right) = 1.25\left(1+\frac{55.7}{3}\right) = 24.46 \quad (\text{V}) \tag{3.4}$$

3.2.2 Excitation Current Design

As listed in Table 3.1, the selected accelerometer requires an excitation current ranging from 2mA to 20mA. Thus, a constant current circuit will be designed to meet this requirement. Here, we choose 4mA as the magnitude of excitation current, is determined based on the available laboratory equipment and by practical application experience. This value is a reference quantity only and is not an expected value for the 603C01 sensor. By investigation, LM334 (from Texas Instrument) is selected as the core chip to design the constant current circuit. Figure 3.3 shows the primary circuit structure of the constant current circuit.

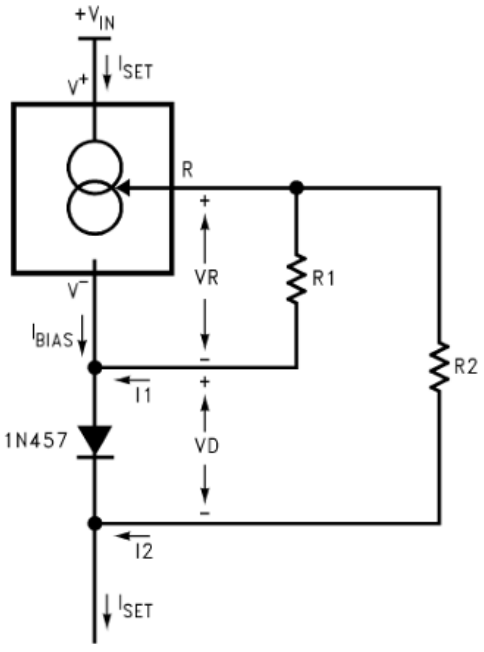

Figure 3.3: The structure of the constant current circuit [61].

The output of the circuit [62] depends on the values of R_1 and R_2 from the following equation:

$$I_{SET} = I_1 + I_2 + I_{BIAS}$$
$$= \frac{V_R}{R_1} + \frac{V_R + V_D}{R_2} \approx \frac{67.7\text{mV}}{R_1} + \frac{67.7\text{mV} + 0.6\text{V}}{R_2} \quad (3.5)$$

In this case, the value for I_{SET} is 4mA. V_R is a constant voltage depending on the temperature [62], which is approximately 64mV under 24.85°C. Besides, V_R needs to consider 5.9% for the I_{BIAS} so that the finally voltage cross resistor R_1 is 67.7mV, or 64mV + 5.9% to account for I_{BIAS}. In addition, based on Eq. (3.5), we need to presuppose a resistance value for R_1. Then, the resistance of resistor R_2 can be calculated by Eq. (3.5). If $R_1 = 20\Omega$, from Eq. (3.5), the value of R_2 can be determined by

$$I_{SET} \approx \frac{67.7\text{mV}}{R_1} + \frac{67.7\text{mV} + 0.6\text{V}}{R_2}$$
$$4 \approx \frac{67.7}{20} + \frac{67.7 + 0.6}{R_2}$$
$$R_2 = \frac{67.7 + 0.6}{4 - \frac{67.7}{20}} = 1085.69 \ \ (\Omega) \quad (3.6)$$

With the calculated value of R_2= 1085.69Ω, which can be approximated as 1kΩ, the current can be updated using Eq. (3.5) or

$$I_{SET} \approx \frac{67.7\text{mV}}{20} + \frac{67.7\text{mV} + 0.6\text{V}}{1000} \approx 3.385 + 0.6677 \approx 4.05 \ \ (\text{A}) \quad (3.7)$$

3.3 Signal Conditioning

The collected vibration signal from the sensing unit needs to be preprocessed before digitization. The processing procedures mainly include amplification and filtering of the signal. In this section, the detailed design of amplifier circuit and filter circuit will be discussed.

3.3.1 Signal Amplification

The used vibration sensor 603C01 has a sensitivity of 100mV/g [58]. This means that the vibration signal collected by the sensor will have a very voltage in amplitude. To better analyze and extract useful information from the collected signals, the signal should be amplified through a signal conditioning circuit in this DAQ system. The primary operational amplifier (Op-Amp) (OP07 from Analog Device) will be used to construct signal conditioning circuit. Table 3.2 summarizes the related parameters of OP07 Op-Amp [63].

Table 3.2: Op-Amp OP07 performance characteristics [63].

Parameter	Specification
Supply Voltage	±22V
Differential Input Voltage	±30V
Slew Rate	0.3V/μs
Close-Loop Bandwidth	0.6MHz
Input Offset Voltage	85μV
Common-Mode Rejection Ratio	120dB
Temperature Range	-40 to +85°C

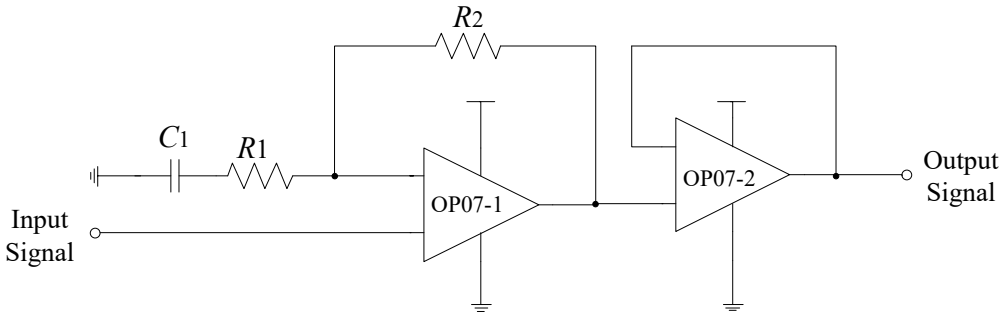

Figure 3.4: The structure of the amplifier circuit.

Figure 3.4 shows the designed amplifier circuit. The first Op-Amp (OP07-1) is a non-inverting AC amplifier to enhance the original signal. The circuit gain can be calculated by:

$$A_V = 1 + \frac{R_2}{R_1} \tag{3.8}$$

In this design, the gain is selected as $A_V = 11$, thus the values of $R_1 = 15\text{k}\Omega$ and $R_2 = 150\text{k}\Omega$ are selected to meet the gain requirement. In addition, the signal input is made up of two parts: the first part is a 12V static DC bias; the second part is the dynamic AC vibration signal. Since the input is an AC signal, capacitor C_1 is used as a coupling capacitor to pass-through AC signal only, which can help isolate the DC bias settings from the sensor. Moreover, the second Op-Amp (OP07-2) is a voltage follower to isolate the first Op-Amp circuit and the following ADC circuit in the DAQ system.

3.3.2 Signal Filter

In real measurement, there is usually a large amount of noise and interference coupled into the circuit, which will degrade the DAQ accuracy. To reduce distortion, a filter is designed and implemented to remove the noise before ADC operation. In this project, we are using a second order Butterworth low-pass filter and a high-pass filter to preprocess the signal. The design filter circuit is shown in Figure 3.5.

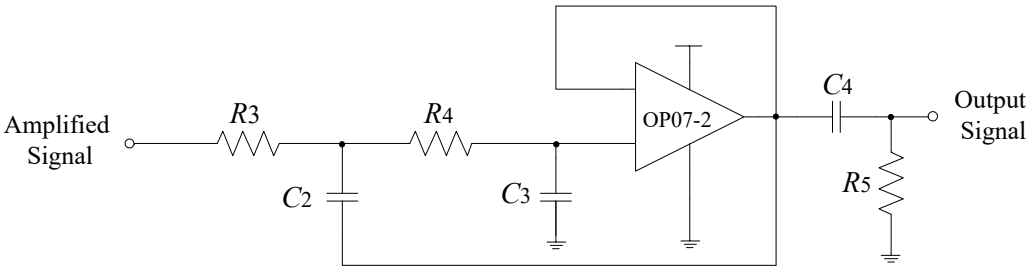

Figure 3.5: The structure of the filter circuit.

In Figure 3.5, R_3, R_4, C_2, and C_3 form the second order Butterworth low-pass filter. Since the sensor bandwidth is between 0.5 Hz and 10 kHz [58], based on bearing fault detection purpose, the cut-off frequency for the low-pass filter is selected as 10 kHz. Based on analysis, the selected components parameters are $R_3 = 1\text{k}\Omega$, $R_4 = 2\text{k}\Omega$, $C_2 = 10\text{nF}$, and $C_3 = 10\text{nF}$. The implemented cut-off frequency of the low-pass filter will be

$$f_c = 1/(2\pi\sqrt{R_3 R_4 C_2 C_3}) \approx 11260 \quad \text{(Hz)} \tag{3.9}$$

which is closed to the expected cut-off frequency 10 kHz.

A high-pass filter is designed to remove some low frequency components and the DC bias to prevent the output signal exceeding the conversion scale of the ADC chip. The selected cut-off frequency for the high-pass filter is 0.5 Hz based on the Table 3.1. It is composed of C_4 and R_5. By trial and error, we have selected R_5 = 670kΩ and C_4 = 22nF. The implemented high pass filter cut-off frequency will be:

$$f_{c(updated)} = 1/(2\pi\sqrt{R_5 C_4}) \approx 1.312 \quad \text{(Hz)} \tag{3.10}$$

3.4 ADC Unit

The primary purpose of ADC within a DAQ system is to convert the analog signals into a digital counterpart for display, storage, transmission and analysis. Normally, a DAQ system uses the internal ADC built in the MCU. For example, in the Sengoz's RF-based DAQ design [18], it uses a 10-bits internal ADC from ATmega328p. In the procedures of the signal from analog to digital, ADC module should ensure converted signal accuracy and integrity. If ADC resolution is only 10 bits, then it will be 5mV per bit under 2.5V reference voltages. If the sensor sensitivity is 100mV/g based on the datasheet of 603C01 [58], then the signal cannot be converted accurately if the vibration magnitude is under 0.05g. Hence, it is essential to increase the resolution of the ADC to convert a wider range of signal components. In addition, most of MCU built-in ADCs do not include differential inputs, which can cause environmental noise to interfere with the circuit and the input signal, thus affecting the quality of DAQ output. Therefore, to ensure the accuracy and integrity of the frequency characteristics of the bearing fault signal, selecting an external ADC for the designed DAQ system design is necessary.

In this research, we will use an external ADC chip ADS131a04 (from Texas Instruments). It has four-channel differential inputs, with 24-bit Delta-Sigma ADC. Its speed can reach up to 128 kilo samples per second (ksps). ADS131A04 has a flexible analog power supply option and can be powered by a unipolar supply between 3.3 V and 5.5 V. In this project, the

ADC power will be provided by the MCU directly. In design, we will use synchronous master mode in the ADS131A0x device as the master and use the MCU as the slave to read the data after each conversion. Devices in synchronous master mode and asynchronous interrupt mode can be used to synchronize the conversions for slave devices in synchronous slave mode [64]. Figure 3.6 illustrates the connection approach and the circuit design.

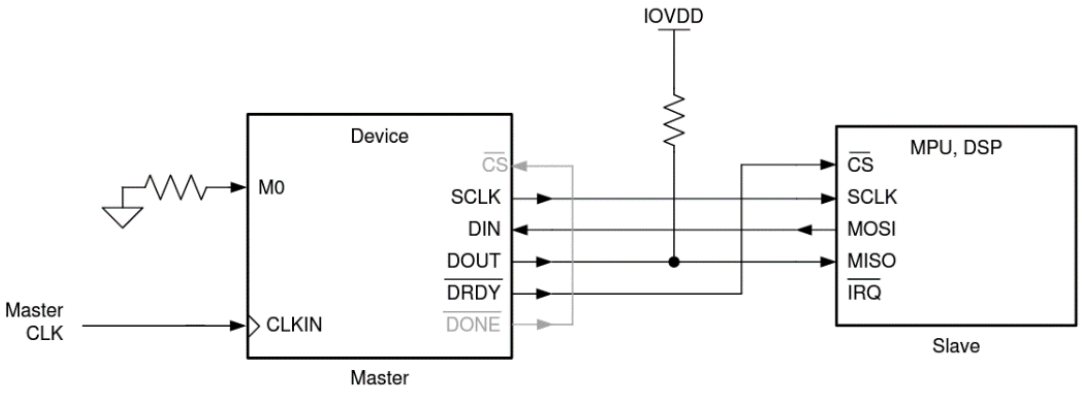

Figure 3.6: Synchronous master mode connection [64].

In general, the ADS131a04 device operation is controlled and configured through a series of commands as listed in the datasheet [64]. The command will be transmitted through SPI with MCU or other host devices. The commands are stand-alone, 16-bit words and reside in the first device word of the data frame. We can write zeroes to the remaining LSBs when operating in 24-bit or 32-bit word sizes because each command has 16-bits in length. The commands are decoded following the completion of a data frame. Each recognized command is acknowledged immediately with a status output in the first device word of the following data frame. ADC initialization is an important procedure in this DAQ system. During the initialization programming, it should enter UNLOCK command 0x0655 and the WAKEUP command 0x0033. By receiving the feedback command 0x0655 from the ADC, the connection status between the host device and the ADC can be determined.

3.5 MCU

The MCU is a transit station in the DAQ system, which is responsible to control operations of different preprocessing units and transmission of data from the ADC to the computing device. As discussed in Section 3.4, the ADC can reach 100ksps with 24-bits

resolution, which means the MCU must have sufficient capability and high operation speed to transmit such massive amount of data. Therefore, it is imperative to choose an appropriate MCU compatible with the ADC. The selected MCU is the ESP32-S2 (from ESPRESSIF Inc.) [65]. It has integrated Wi-Fi connectivity based on ESP8266 that can be used in Internet of Things (IoT) applications. The specific features of ESP32-S2 are listed in Table 3.3.

Table 3.3: ESP32-S2 performance and characteristics [65].

Parameter	Specification
CPU	Xtensa® single-core 32-bit LX7
SRAM	320 KB
ROM	128 KB
GPIOs	43
Operation Speed	240 MHz
USB	One Full Speed USB OTG
SPI	4

The selected EPS32-S2 has a 240MHz operation speed and a USB interface, which can match the performance of the high-speed ADC (ADS131a04). Figure 3.7 displays the connection approach for the MCU and ADC for wired data transmission with a PC.

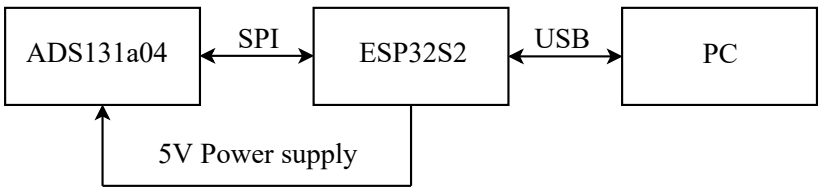

Figure 3.7: ADC-MCU connection module.

In addition, C++ language is used for programming. The development environment is the Arduino IDE, which has some extra benefits such as available libraries for SPI and serial communication. The SPI setup is initialized through SPI libraries. The ADC initialization commands mentioned in Section 3.4 are converted to C++ code and added to the SPI libraries.

3.6 Digital Switch Unit

Since the accelerometer is a battery powered IEPE sensor, energy saving modes should be considered in the circuit design. To save power, when the MCU is not collecting data, the power circuit should automatically be turned off. We will use one of the GPIOs of ESP32-s2 to operate a MOSFET as a switch to control the power supply circuit of the IEPE sensor. Figure 3.8 shows the basic structure of digital switch circuit.

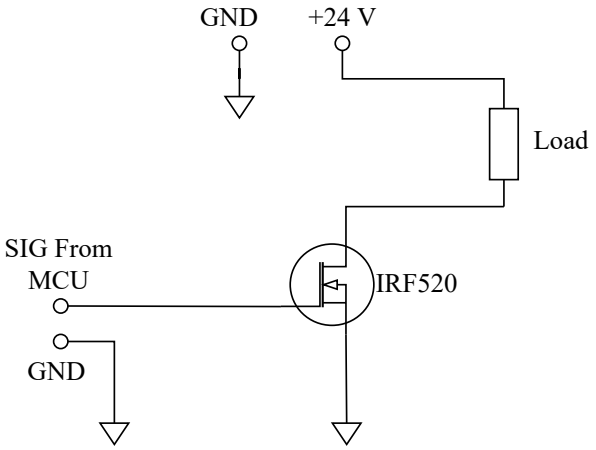

Figure 3.8: Basic structure of digital switch circuit.

IRF520 (from Vishay Siliconix) is selected as the MOSFET component, whose primary parameters are listed in Table 3.8. Since the required voltage of the sensor is 24V and the current is 4mA, the power consumption of the sensor is 0.096W, which is low in power consumption. Therefore, the power provided by the battery can still meet the power requirements of the sensor, while the dissipation on the MOSFETs can be negligible.

Table 3.4: IRF520 typical parameters [66].

Parameter	Specification
R_{DS} (V_{DS}=10V)	0.25
V_{DS}	100V
$Q_{G.max}$	16nC
Q_{gs}	4.4nC
Q_{gd}	7.7nC

In circuit design, the digital switch is controlled by using a Wi-Fi function. The MCU can generate a local web server that can be accessed by any PC or mobile phone. The only limitation to access this local web server is that the user device needs to be connected to the same wireless network or Wi-Fi with the MCU. Figure 3.9 shows the related web control interface.

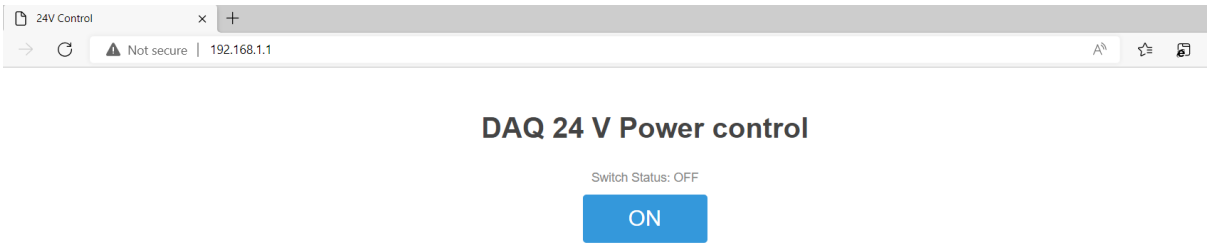

Figure 3.9: Digital switch web control interface

3.7 Verification of the Developed DAQ System

To examine the effectiveness of the developed wired DAQ system, some experimental tests are undertaken using the experimental setup as shown in Figure 3.10. The experiment setup consists of an excitation shaker connected to the power amplifier. The frequency generator controls the shaking frequency. An IEPE vibration sensor (ICP-603C01) is mounted on the platform of the excitation shaker to measure the vibration signals along the vertical axis.

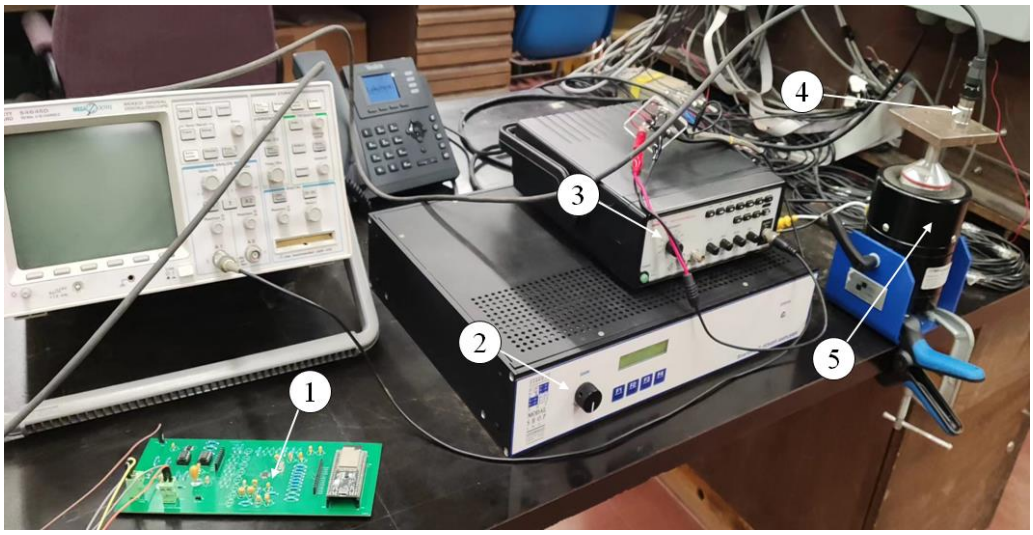

Figure 3.10: Experimental Setup: (1) tested DAQ system; (2) Power amplifier; (3) Frequency generator; (4) ICP vibration sensor; (5) Excitation shaker.

Four different frequencies of 30 Hz, 3 kHz, 6 kHz, and 9 kHz are used in this test. The sampling rate is set at 10ksps. In testing, firstly, the shaker generates the required vibration signal, and the sensor collects and transmits the analog signal to the DAQ system, which is then transmitted to the PC via serial communication. For testing, these data are analyzed using MATLAB.

Figure 3.11 shows some processing results using the FFT corresponding to excitation frequencies of (a) 28.5 Hz; (b) 2.88 kHz; (c) 5.85 kHz; (d) 8.67 kHz, respectively. It is clear that these excitation frequencies can be recognized accurately. Some minor errors in reading are because when using the knob of the signal generator to set the excitation frequency, the panel reading may not be very accurate.

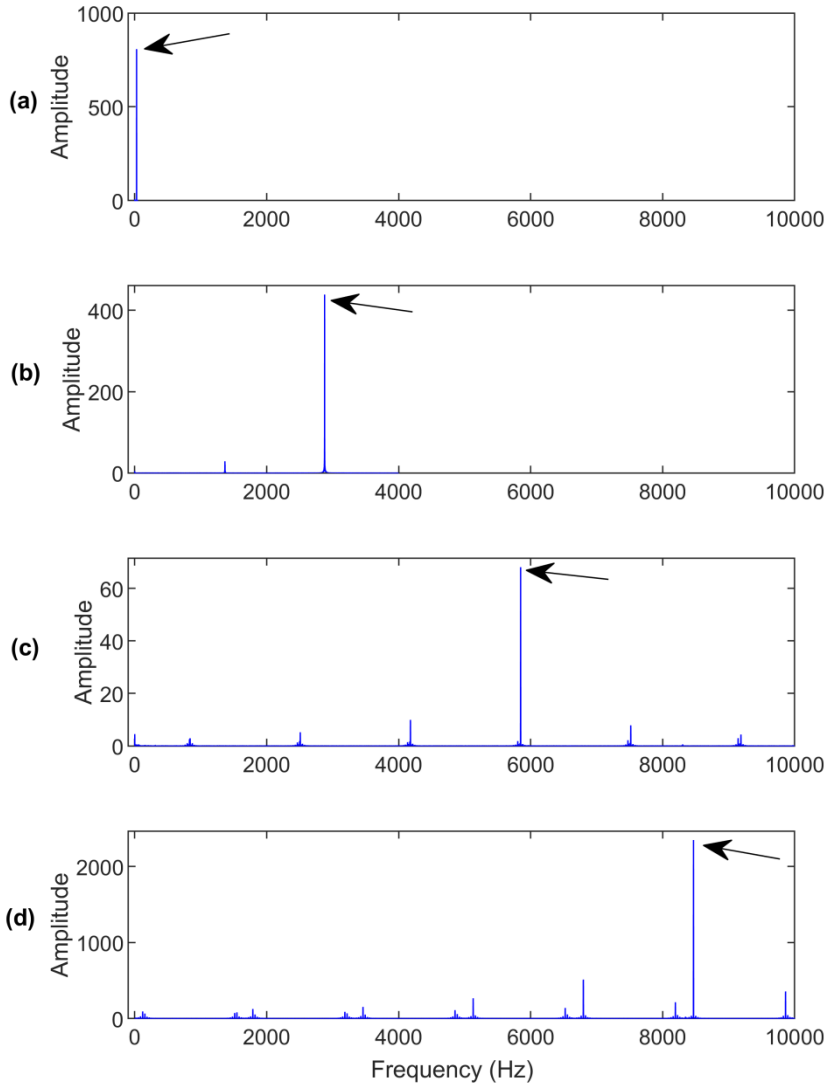

Figure 3.11: The processing result of DAQ system under different test frequencies: (a) 28.5 Hz; (b) 2.88 kHz; (c) 5.85 kHz; (d) 8.67 kHz.

3.8 User Interface

To facilitate DAQ system control and data communication, a user interface is developed using LabVIEW, as shown in Figure 3.12. The serial port driver included in the LabVIEW library can help connect to the MCU to get data. In the interface, the serial port parameters van be reconfigurable. In Figure 3.12, the represented serial communication parameters include port number, baud rate, parity, and stop bit and those parameters need to be setup by user in advance.

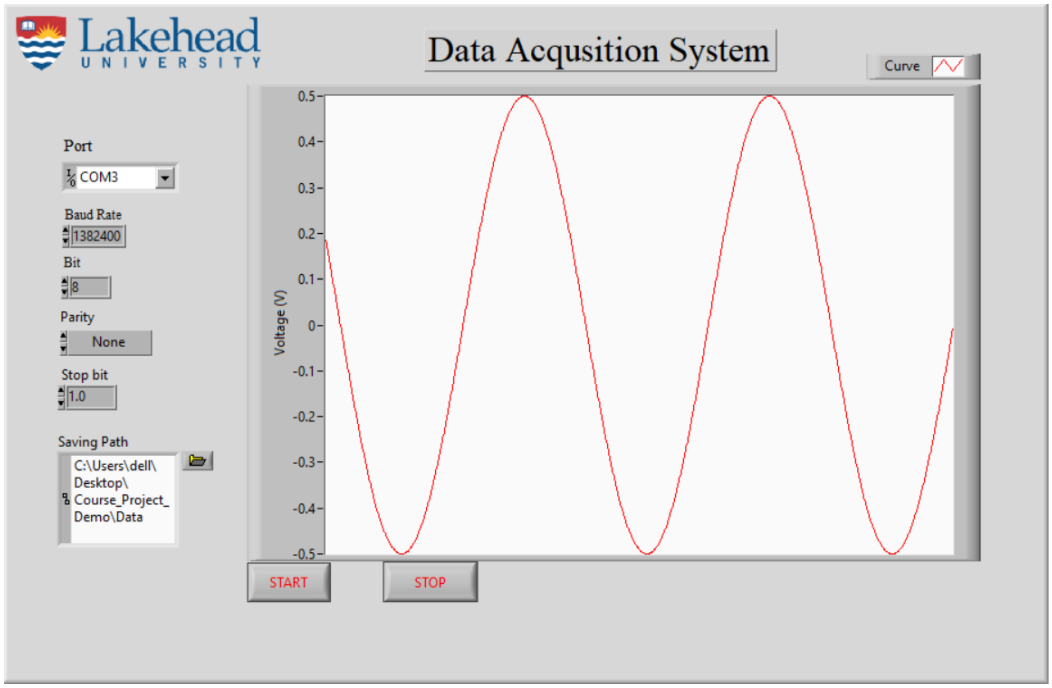

Figure 3.12: DAQ user interface.

In addition, after setting the save path, the image data can be saved directly to an Excel file. Figure 3.13 lists part of the saved data sets from the DAQ interface platform.

Name:DAQ1			
CH1	CH2	CH3	CH4
-0.15937	0.002722	0.003632	0.002814
-0.15911	0.003012	0.003905	0.003115
-0.15886	0.002766	0.003842	0.002984
-0.15822	0.001972	0.002878	0.002075
-0.15754	0.001409	0.002355	0.001444
-0.15693	0.001252	0.002188	0.001327
-0.15605	0.001098	0.001985	0.001066
-0.15528	0.001417	0.002424	0.001565
-0.15437	0.002087	0.002953	0.002109
-0.15357	0.002425	0.003404	0.00253
-0.15246	0.002575	0.003383	0.002605
-0.15152	0.001684	0.002688	0.001862
-0.15044	0.001067	0.001942	0.001135
-0.14936	0.000877	0.001787	0.001002
-0.14834	0.000742	0.001585	0.000757

Figure 3.13: Part of the saved data in Excel by using the DAQ interface.

In addition, based on the features of the LabVIEW environment, it can generate an installation software for the DAQ interface. This installation software can install the DAQ control package on the PC without installing LabVIEW.

3.9 Summary

In this chapter, the MCU-based DAQ system with a high speed and high resolution design has been designed and analyzed. The DAQ system consists of the sensor unit, the power supply module, the signal conditioning module, ADC, and MCU. The vibration sensing unit is selected in this research. A boost converter module and a constant current source module are designed to meet the sensor voltage and current requriements. A signal conditioning module is designed for signal amplification and filtering. An external ADC unit is designed to meet the requirements of the high sampling rate and high resolution. Some primary tests have been undertaken to verify the accuracy of the developed DAQ system.

Chapter 4

Adaptive Variational Mode Decomposition (AVMD) for Bearing Fault Detection

The proposed AVMD technique in this chapter is for modulation of irregular frequency components in signals and for bearing fault detection. It aims to provide more efficient bearing health monitoring. The details will be discussed in this chapter.

4.1 Principle of Variational Mode Decomposition Theory

Variational mode decomposition (VMD) is a non-recursive analysis technique for signal decomposition [67]. In this study, VMD is applied to extract the bearing fault characteristic features from the vibration signal.

In the VMD technique, it is assumed that the original signal can be decomposed into several modes, and each mode is a signal with a narrow-band and located around a center frequency [67]. The instinct mode function (IMF) $u_k(t)$ represents an amplitude-modulated and frequency-modulated signal, which can be expressed as:

$$u_k(t) = A_k(t) \times \cos(\phi_k(t)) \tag{4.1}$$

where k represents the k-th IMF, $A_k(t)$ denotes the instantaneous amplitude, and $\phi_k(t)$ denotes the phase.

The fundamental equation of VMD can be expressed by solving the constrained variational problem in Eq. (4.2):

$$\begin{aligned} \min_{\{u_k\},\{\omega_k\}} \left\{ \sum_{k=1}^{K} \left\| \partial_t \left[\left(\delta(t) + \frac{j}{\pi t} \right) * u_k(t) \right] e^{-j\omega_k t} \right\|_2^2 \right\} \\ \text{s.t.} \quad \sum_{k=1}^{K} u_k(t) = f(t) \end{aligned} \tag{4.2}$$

where K is the IMF number; u_k and ω_k denotes the k-th IMF and its corresponding

center frequency; ∂_t denotes the partial derivative of time; $\delta(t)$ denotes the Dirac delta distribution; $f(t)$ is the original input signal; j is the complex number; * is the convolution operator.

To solving the constrained variation problem of Eq. (4.2), the augmented Lagrangian method [68] can be used to covert Eq. (4.2) into an unconstrained optimization problem, which can be rewritten as:

$$\begin{aligned}\mathcal{L}\left(\{u_k\},\{\omega_k\},\lambda\right) &:= \alpha\sum_k \left\| \partial_t \left[\left(\delta(t) + \frac{j}{\pi t} \right) * u_k(t) \right] e^{-j\omega_k t} \right\|_2^2 \\ &+ \left\| f(t) - \sum_k u_k(t) \right\|_2^2 + \left\langle \lambda(t), f(t) - \sum_k u_k(t) \right\rangle \end{aligned} \tag{4.3}$$

where α is the quadratic penalty factor, $\lambda(t)$ is Lagrangian multiplier coefficient, and $f(t)$ is the original input signal.

In order to obtain an optimal solution of the unconstrained problem in Eq. (4.3), an alternated direction method of multipliers proposed in [68] can be used for analysis. The unconstrained problem in Eq. (4.3) can be transferred into two equivalent minimization problems based on alternated direction method of multipliers. Thus, modes u_k and their corresponding center frequency ω_k can be updated as:

$$u_k^{n+1} \leftarrow \arg\min_{u_k} \mathcal{L}\left(\left\{u_{i<k}^{n+1}\right\},\left\{u_{i\geq k}^{n}\right\},\left\{\omega_i^n\right\},\lambda^n\right) \tag{4.4}$$

$$\omega_k^{n+1} \leftarrow \arg\min_{\omega_k} \mathcal{L}\left(\left\{u_i^{n+1}\right\},\left\{\omega_{i<k}^{n+1}\right\},\left\{\omega_{i\geq k}^{n}\right\},\lambda^n\right) \tag{4.5}$$

Based on Eq. (4.4), the problem can be rewritten as the following equivalent minimization problem:

$$\begin{aligned} u_k^{n+1} = \arg\min_{u_k \in X} \Bigg\{ & \alpha \left\| \partial_t \left[\left(\delta(t) + \frac{j}{\pi t} \right) * u_k(t) \right] e^{-j\omega_k t} \right\|_2^2 \\ & + \left\| f(t) - \sum_i u_i(t) + \frac{\lambda(t)}{2} \right\|_2^2 \Bigg\} \end{aligned} \tag{4.6}$$

Using Parseval/Plancherel Fourier isometry under the L^2 norm and the Hermitian symmetry of the Fourier transform (FT) of the real signal, Eq. (4.6) can be solved in the spectrum domain, such that:

$$\begin{aligned}\hat{u}_k^{n+1} = \arg\min_{\hat{u}_k, u_k \in X} \Bigg\{ & \int_0^{\infty} 4\alpha \left(\omega - \omega_k\right)^2 \left|\hat{u}_k(\omega)\right|^2 \\ & + 2 \left| \hat{f}(\omega) - \sum_i \hat{u}_i(\omega) + \frac{\hat{\lambda}(\omega)}{2} \right|^2 d\omega \Bigg\}\end{aligned} \tag{4.7}$$

After the first variation in the positive frequency vanishes, the solution of this quadratic optimization problem becomes:

$$\hat{u}_k^{n+1}(\omega) = \frac{\hat{f}(\omega) - \sum_{i \neq k} \hat{u}_i(\omega) + \frac{\hat{\lambda}(\omega)}{2}}{1 + 2\alpha \left(\omega - \omega_k\right)^2} \tag{4.8}$$

which can be considered as a Wiener filter to process current residual [66], with a signal prior $1/\left(\omega - \omega_k\right)^2$.

In addition, for Eq. (4.5), the reconstruction term of center frequencies ω_k is:

$$\omega_k^{n+1} = \arg\min_{\omega_k} \left\{ \left\| \partial_t \left[\left(\delta(t) + \frac{j}{\pi t} \right) * u_k(t) \right] e^{-j\omega_k t} \right\|_2^2 \right\} \tag{4.9}$$

Similarly, the optimization of the center frequency can also be performed in the Fourier domain, by optimization the following function:

$$\omega_k^{n+1} = \arg\min_{\omega_k} \left\{ \int_0^{\infty} \left(\omega - \omega_k\right)^2 \left|\hat{u}_k(\omega)\right|^2 d\omega \right\} \tag{4.10}$$

This quadratic optimization problem can be solved as:

$$\omega_k^{n+1} = \frac{\int_0^{\infty} \omega \left|\hat{u}_k(\omega)\right|^2 d\omega}{\int_0^{\infty} \left|\hat{u}_k(\omega)\right|^2 d\omega} \tag{4.11}$$

Moreover, the Lagrangian multiplier $\lambda(t)$ can be updated by:

$$\hat{\lambda}^{n+1}(\omega) = \hat{\lambda}^{n}(\omega) + \tau\left(\hat{f}(\omega) - \sum_{k}\hat{u}_{k}^{n+1}(\omega)\right) \tag{4.12}$$

where τ is the iteration step size.

The iteration will be completed until the accuracy meets the following convergence criterion:

$$\sum_{k}\left\|\hat{u}_{k}^{n+1} - \hat{u}_{k}^{n}\right\|_{2}^{2} / \left\|\hat{u}_{k}^{n}\right\|_{2}^{2} < \epsilon \tag{4.13}$$

where ϵ is the convergence threshold used to control the reconstruction of each mode.

In processing, the steps of the VMD algorithm are summarized as follows:

Step 1: Initialize $\left\{\hat{u}_{k}^{1}\right\}$, $\left\{\omega_{k}^{1}\right\}$, $\hat{\lambda}^{1}$, and $n = 1$

Step 2: Calculate $\hat{u}_{k}$ and ω_{k} based on Eq. (4.8) and Eq. (4.11), respectively, k = 1, 2, …. K.

Step 3: Update $\hat{\lambda}$ in Eq. (4.12).

Step 4: Repeat Steps 2-3 until the iteration meets the criterion in Eq. (4.13).

Step 5: Compute the K mode components u_{k}.

The parameters K, α, τ, and ϵ need to be selected based on applications through error and trial procedures [69]. Specifically, K and α have a direct influence on the calculation results in the VMD algorithm. $\tau = 0$, $\epsilon = 1\times10^{-6}$ are selected in this case. Advanced research will be undertaken in the future to select these values analytically.

4.2 Cross-Correlation

Before using VMD for decomposition, the parameter K (i.e., IMF number) needs to be selected in advance. Usually, the magnitude of the K value is set by experience or speculation. If K is too small, extra signal components may appear in one mode, whereas some components become unpredictable. Conversely, if K is too large, some components will appear in more than one mode and the frequencies of the modal centers will overlap [70]. Therefore, setting a suitable K value is important in the VMD algorithm, which should be selected properly to further improve the accuracy of the final decomposed modes.

In proposed AVMD, the magnitude of *K* will be determined by the correlation between signals and decomposed modes. In signal processing, cross-correlation is a measure of similarity between two or more time series data sets. Accordingly, the correlation between the original input signal and sum of the decomposed modes can be calculation by

$$\rho_{xy} = \frac{C_{xy}}{\sigma_x \sigma_y} \tag{4.14}$$

where x is the sum of the modes; y is the original signal; C_{xy} is the cross-covariance function; σ_x and σ_y are the standard deviations of x and y, respectively. The cross-correlation ρ_{xy} represents the correlation between the integration of the decomposed modes and the original signal; the larger ρ_{xy}, the higher the correlation between two signals [71].

For illustration, a simple example will be used for cross-correlation simulation. The modulated signals are defined as follow:

$$y_1(t) = \sin(2\pi \times 200t) \tag{4.15}$$

$$y_2(t) = \sin(2\pi \times 300t) \tag{4.16}$$

$$y_3(t) = \sin(2\pi \times 400t) \tag{4.17}$$

$$y(t) = y_1(t) + y_2(t) + y_3(t) \tag{4.18}$$

Based on Eq. (4.14), a simulation result of cross-correlation corresponding to different *K* is shown in Figure 4.1.

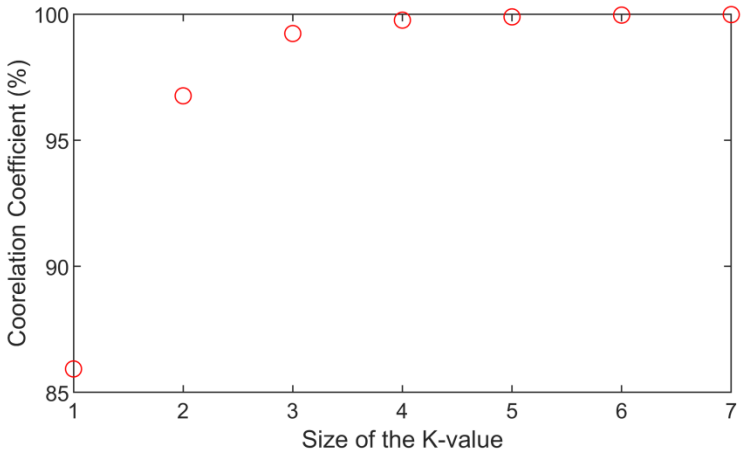

Figure 4.1: The cross-correlation between the original signal and different K values.

Since the modulated signal is composed of three parts, the modes decomposed by the VMD should also have three modes theoretically. As shown in Figure 4.1, when $K = 2$ and 3, the correlation coefficients are 96.85% and 99.23%, respectively. Therefore, the signal is under decomposition for $K = 2$. When $K = 4$ and 5, the correlation coefficients are 99.76% and 99.89%, respectively. Although these correlation coefficients are higher than that in $K = 3$, the results of $K = 3$ are still selected as the final result to avoid possible overlapping, which may degrade the accuracy of mode decomposition. Figures 4.2 and 4.3 show two example spectra of the modulated signal when $K = 2$ and 3, which can help to analyze the overlap situation.

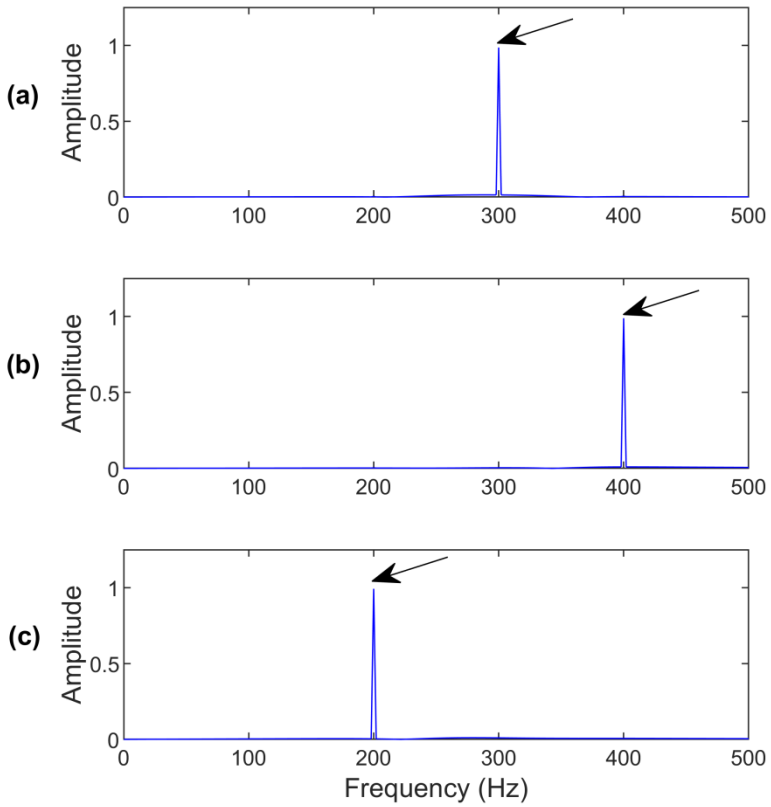

Figure 4.2: Frequency spectrum when $K = 3$ and center frequency for each mode: (a) $f_{\mathrm{IMF1}} = 300$ Hz; (b) $f_{\mathrm{IMF2}} = 400$ Hz; (c) $f_{\mathrm{IMF3}} = 200$ Hz.

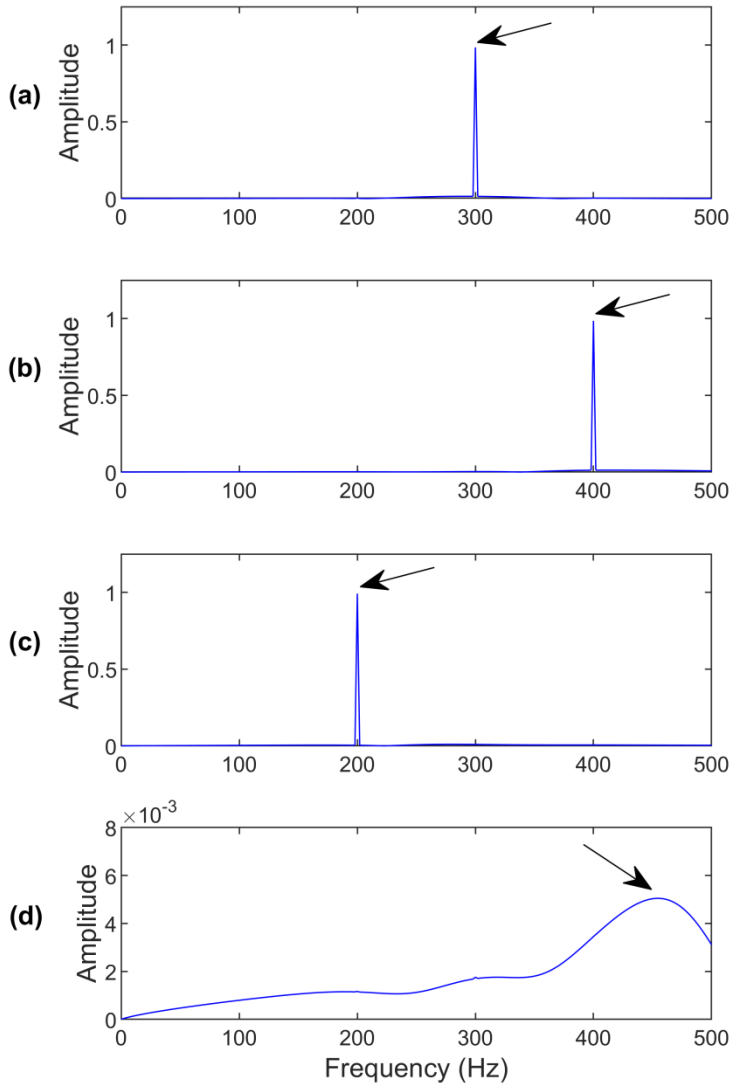

Figure 4.3: Frequency spectrum when K = 4 and center frequency for each mode: (a) f_{IMF1} = 300 Hz; (b) f_{IMF2} = 400 Hz; (c) f_{IMF3}=200 Hz; (d) f_{IMF4} = 458 Hz.

Compared Figure 4.2 with Figure 4.3, it is clear that when K value is over the number of original signal components, additional frequency components will generated due to overlapping effect as shown in Figure 4.3 (d). The presence of these additional frequency components will reduce IMF2 magnitude, which will affect the accuracy of the IMF2. Therefore, based on this simulation results, it is concluded that the correlation of 99% will be set as a threshold as a basis for selecting the K value to avoid overlapping occurrence in the propose AVMD technique.

4.3 Determination of the Penalty Factor

Based on the discussion in Section 4.1 and literature [67], the function of the penalty

factor α can be used to determine the bandwidth of mode component. In general, a constant penalty factor can be selected and used in following VMD mode calculations. Generally, a larger penalty factor will generate the narrower bandwidth of the mode component; otherwise, a smaller penalty factor will result in a wider the bandwidth of the mode component. According to the characteristics of the spectrum distribution of a vibration signal, most bearing fault characteristic frequencies and their harmonics are located over the low and medium frequency region [72]. Therefore, the characteristics of the signal's center frequency can be used to determine the penalty factor corresponding to each mode used for VMD signal decomposition and achieve the adaptive selection for the penalty factor in proposed AVMD technique. The detail of how to adaptively select penalty factors will be introduced below.

When the center frequency of the decomposed mode is low, the mode components are mainly harmonics in the low and medium frequency bandwidths; then a larger penalty factor can be chosen, and vice versa. Eq. (4.19) is an empirical formula to approximately determine the penalty factor [73]:

$$\alpha_k = \left(\frac{1}{1+e^{\log_{10}\frac{2f_{kc}}{f_s}}} - 0.5 \right) \cdot \frac{f_s}{2} \tag{4.19}$$

where α_k is the penalty factor and f_{kc} is the center frequency corresponding to *k*-th mode component, respectively; f_s is the sampling frequency. f_{kc} can be calculated by

$$f_{kc} = \frac{\sum_{i=1}^{N/2} [i \cdot f_s / N \cdot |U_k(i)|^2]}{\sum_{i=1}^{N/2} |U_k(i)|^2} \tag{4.20}$$

where N is the length of the original signal, and U_k is the discrete FT of *k*-th mode component u_k.

By using Eq. (4.19), the penalty factor α_k can be adaptively adjusted according to the frequency characteristics of each decomposed mode.

4.4 Ensemble Kurtosis

In proposed AVMD, once completing the VMD, the next step is to select proper IMFs for signal analysis. In bearing fault detection, fault characteristic frequencies, harmonics, impulses, and noise have different probability densities and statistical properties [74]. Kurtosis is a measure of the tails of the probability distribution function [75]. In practice, kurtosis-based methods tend to focus on the frequency band of individual pulses rather than on the defect impulses, because they only emphasize the impulsivity but ignore the cyclicity. Envelope spectral kurtosis can measure and evaluate the cyclicity [68], which will be adopted in bearing fault diagnosis in this work such that:

$$E_K = E_{KS} \cdot K = \frac{\sum_{p=1}^{P} |\overline{S_E(p)}|^4}{\left(\sum_{p=1}^{P} |\overline{S_E(p)}|^2 \right)^2} \cdot K \tag{4.21}$$

where E_K is the ensemble kurtosis, E_{KS} is envelope spectrum kurtosis, and K is the kurtosis. S_E is the envelope spectrum of signal and P is the sampling number of envelope spectrum.

Figure 4.4 shows a comparison of the related indicators [69]. K_{CI} is the weighted kurtosis index. It is seen that E_K index is sensitive to impulses, which will be used in this work for the selection of IMFs for signal analysis and bearing fault detection.

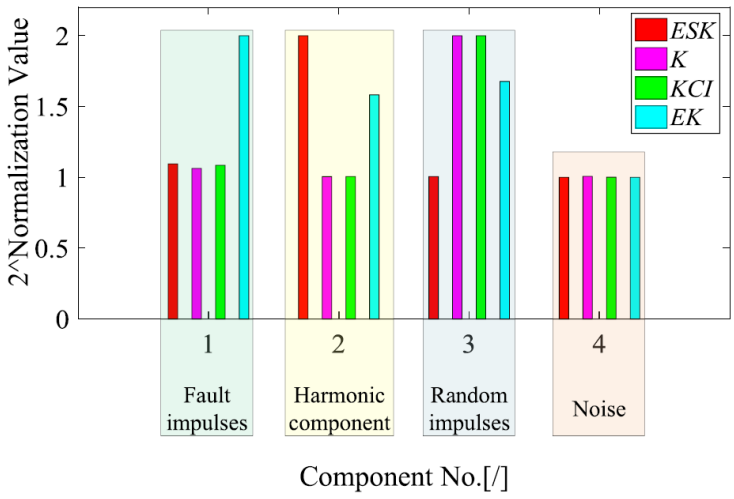

Figure 4.4: The comparison of four indexes when they process different components in the machinery signal [69].

4.5 Envelop Spectrum Analysis

From the AVMD analysis, the selected IMF will be used to extract the fault-related features for envelope analysis and bearing fault detection [76]. The specific signal processing procedures will be discussed as following. Firstly, the analytic signal $a_x(t)$ will be formulated from the signal by using the Hilbert transform, which can be expressed as:

$$a_x(t) = x(t) + j\hat{x}(t) = \sqrt{x^2(t) + j\hat{x}^2(t)} \cdot e^{j\phi_x(t)} = A_x(t)e^{j\phi_x(t)} \tag{4.23}$$

where $x(t)$ is the real part of the amplitude modulated signal; $\hat{x}(t)$ is the Hilbert transform of $x(t)$; $\phi_x(t)$ is the instantaneous phase; and $A_x(t)$ is the instantaneous amplitude.

Secondly, the absolute value of $a_x(t)$ will be used to determine the envelope signature. Thirdly, the envelope spectrum is obtained by taking the FT of the envelope signal. Finally, bearing fault detection is undertaken by examining characteristic frequencies on the envelope spectrum.

When a bearing fault occurs, the fault spots will excite periodic shock impulses in bearing operation, which will modulate bearing signal. Compared to the analysis of the frequency spectrum, the envelope spectrum analysis can demodulate and extract these low frequency impulse signatures. This property will be demonstrated by using the following simulation [77]. The shaft speed is 25 Hz, and characteristic frequency is f_{od} = 83.33 Hz.

Figure 4.5 shows a simulated signal from a bearing with an outer race damage. Its frequency spectrum and envelop spectrum analysis of this bearing outer race fault signal are shown in Figure 4.6. In Figure 4.6(a), the frequency spectrum can only recognize the shaft frequency 25 Hz and its harmonics, but it cannot identify information about the bearing fault characteristic frequency. However, in Figure 4.6(b), the bearing outer race fault frequency f_{od} = 83.33 Hz and its harmonics can be recognized clearly. Thus envelope analysis could provide a better solution for extracting fault features on the decomposed mode using the VMD technique.

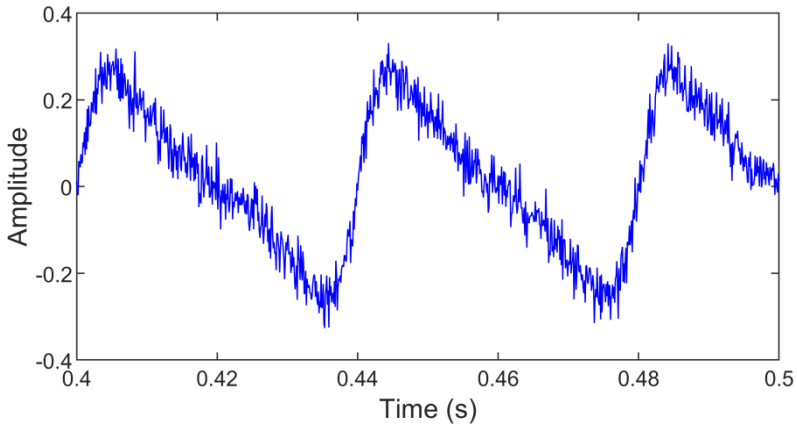

Figure 4.5: Simulated signal from a bearing with outer race fault.

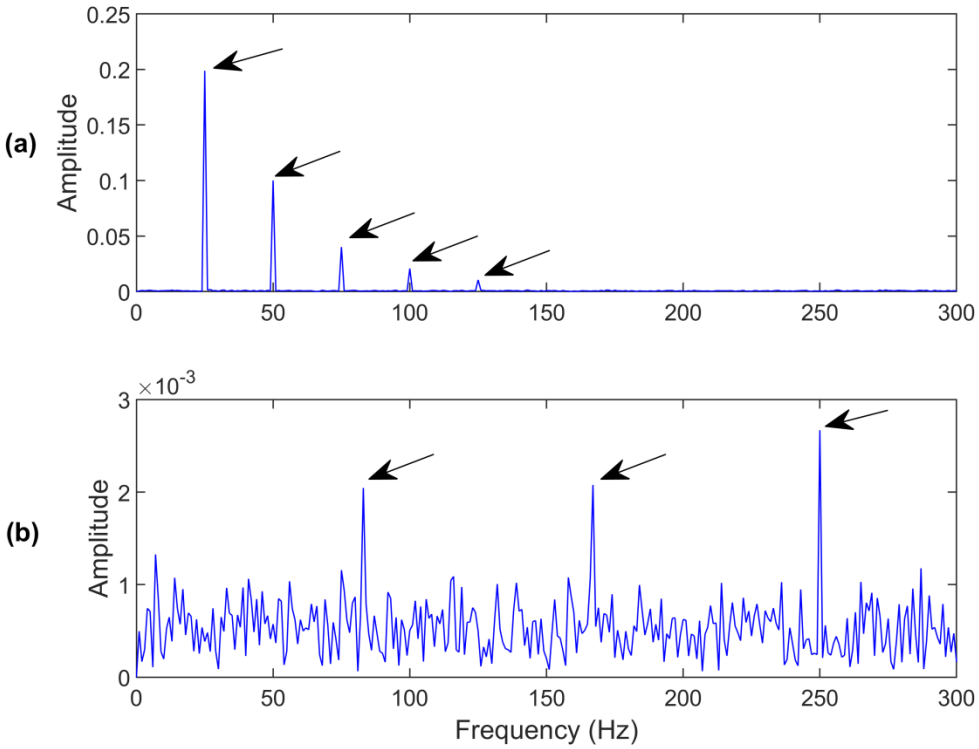

Figure 4.6: Comparison of different spectrum: (a) Frequency spectrum with shaft frequency f_r = 25Hz and its harmonics; (b) Envelop spectrum with outer race fault frequency f_{od} = 83.33 Hz and its harmonics.

4.6 The Proposed Adaptive Variational Mode Decomposition (AVMD)

An AVMD technique will be proposed in this section to extract the impulsive features for bearing fault detection. AVMD will integrate the related approaches as discussed in Section 4.5. Its processing flowchart is presented in Figure 4.7. The main steps of the AVMD are summarized as follows:

Step 1: Initialize system parameters: $K = 1$ and $\alpha = 100$.

Step 2: Run the VMD and compute the correlation using Eq. (4.41). If the correlation is over 99%, proceed to Step 3. Otherwise, let $K = K + 1$ and repeat Step 2.

Step 3: Compute the penalty factor using Eq. (4.14) for each mode.

Step 4: Re-run VMD with the optimal K and α, and compute E_K using Eq. (4.21) for each mode.

Step 5: Analyze the largest E_K mode by the envelope analysis and do bearing fault detection.

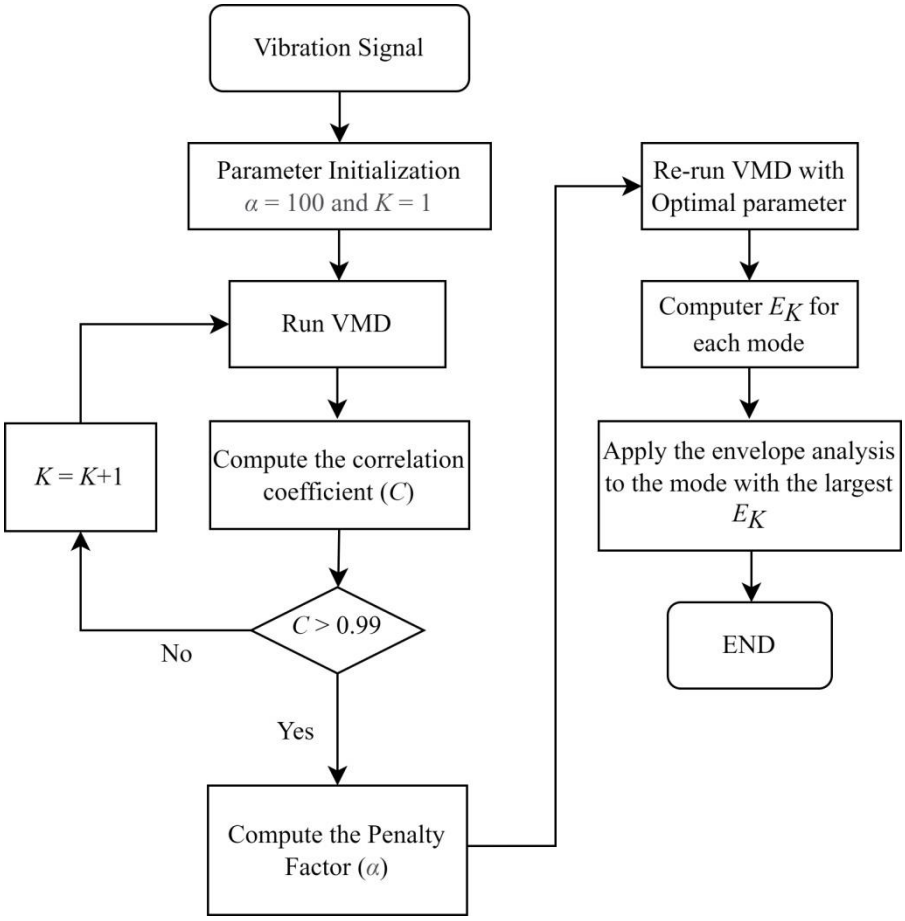

Figure 4.7: The flowchart of AVMD.

4.7 Simulation Test and Analysis

To further verify the effectiveness of the AVMD technique, a simulation test will be illustrated. The simulated signals are defined as follows [78]:

$$y_1(t) = 1.5 \times \sin(2\pi \times 500t) \tag{4.24}$$

$$y_2(t) = 5 \times e^{-0.1 \times 2\pi \times 2000t} \times \sin\left(2\pi \times 2000t \times \sqrt{1-0.1^2}\right) \tag{4.25}$$

$$y_3(t) = 10 \times e^{-0.1 \times 2\pi \times 1200t} \times \sin\left(2\pi \times 1200t \times \sqrt{1-0.1^2}\right) \tag{4.26}$$

$$y(t) = y_1(t) + y_2(t) + y_3(t) + n(t) \tag{4.27}$$

where y_1 are the harmonic components, y_2 are the periodic impulses, y_3 are the aperiodic impulses, y is the modulated signal, and n is the Gaussian noise.

The frequency of a fault impulse is set at 25 Hz. The sampling frequency is 10 kHz, and the signal length is 10 k. The density of Gaussian noise is 0.4. The simulation results of Eq. (4.25)-(4.27) and Gaussian noise are shown in Figure 4.8(a)-4.8(d), separately. The frequency spectrums of corresponding signals are shown in Figure 4.8(e)-4.8(h), respectively.

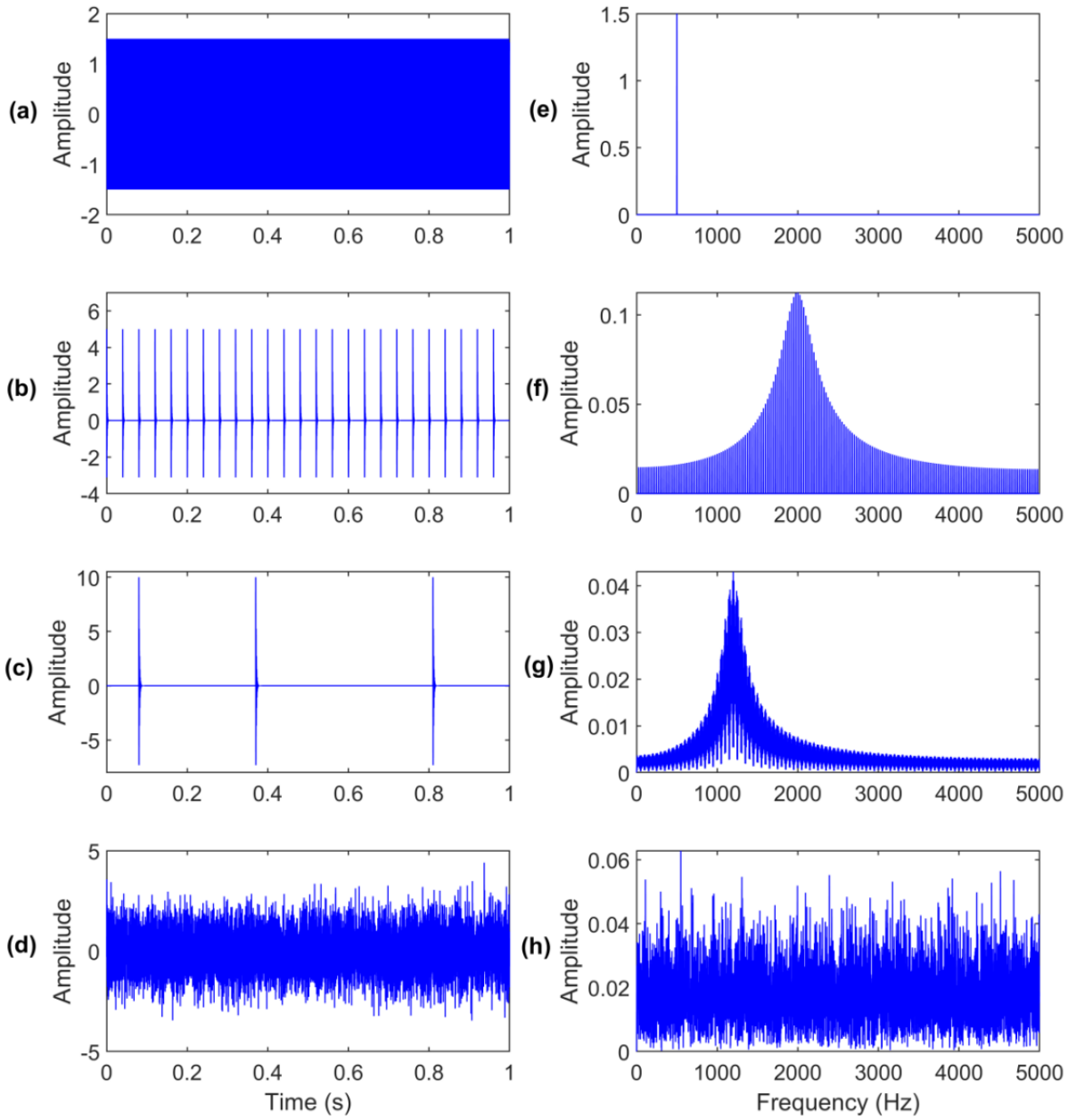

Figure 4.8: Components of the simulation signal: (a) the harmonics; (b) the periodic impulses; (c) the aperiodic impulses; (d) the Gaussian noise. (e) Spectrum of the harmonics; (f) Spectrum of the periodic impulses; (g) Spectrum of the aperiodic impulses; (h) Spectrum of the Gaussian noise.

The proposed AVMD technique is applied to process the simulated signal above, and Figure 4.9 shows the processing results. Figure 4.9(a)- Figure 4.9(c) show the processing results using the AVMD technique, corresponding to IMF1, IMF2 and IMF3, respectively. The corresponding indicator values are 1.91, 10.38, and 3.01. Then IMF2 has the highest E_K index, and will be chosen for envelope analysis. Figure 4.9(d)-4.9(f) depict the resulting envelope spectrums of IMF1, IMF2 and IMF3. It is seen that IMF2 envelope spectrum in

Figure 4.9(e) can clearly recognize the impulse characteristic frequency of 25 Hz and its harmonics. In contrast, the envelope spectra of the other IMFs do not contain sufficient characteristic information. Thus, the simulation results can verify the effectiveness of the AVMD technique to recognize representative features.

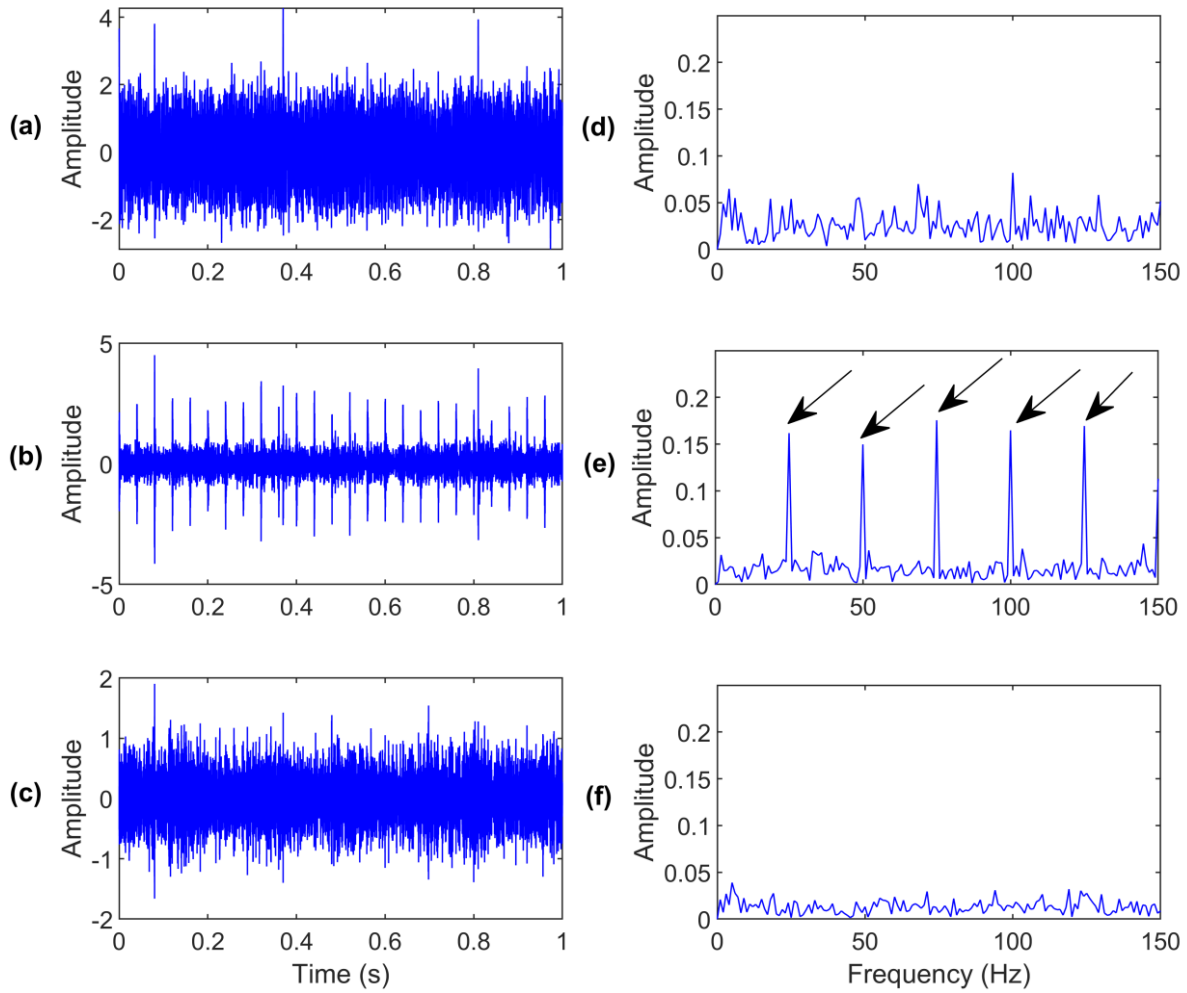

Figure 4.9: The results of AVMD for the simulated signal: (a) IMF1 (E_k = 1.91); (b) IMF2 (E_k = 10.38); (c) IMF3 (E_k = 3.01). (d) Envelop spectrum of IMF1; (e) Envelop spectrum of IMF2; (f) Envelop spectrum of IMF3.

To examine the processing efficiency of the proposed AVMD technique, more simulation tests will be undertaken to compare the number of VMD modes, the iterations and processing time. The related techniques include: Teager operator method [79], particle swarm optimization algorithm [80], and gray wolf algorithm [81]. Table 4.1 summarizes the comparison results of these VMD methods. It can be seen that the AVMD technique has K = 3, which is the same as the results of the particle swarm optimization method and the gray wolf algorithm. However, the AVMD technique takes the lowest number of iterations (114

runs) or the shortest computation time (3.2 sec) to reach convergence, compared with other three related methods, which is a significant advantage in real-time machinery condition monitoring.

Table 4.1: Comparison of the mode number of different VMD methods using the modulated signal.

VMD Method	Number of K	Number of iterations	Calculation time (sec)
Teager operator	4	249	5.3
Particle swarm optimization	3	706	13.1
Gray wolf	3	354	7.2
Proposed AVMD technique	3	114	3.2

Experimental tests will be undertaken in Chapter 5 to further examine the effectiveness of proposed AVMD technique for nonlinear feature analysis and bearing fault detection.

4.8 Summary

A new AVMD technique has been proposed in this chapter for nonlinear signal property analysis. Firstly, the main VMD parameters are adaptively selected using the correlation analysis. Secondly, the VMD operation is optimized to get the decomposed signal. Thirdly, the ensemble kurtosis is used to decompose the signal. Finally, an envelope spectrum analysis is applied to examine the fault characteristic features for bearing fault diagnosis. The effectiveness of AVMD has been verified by simulation tests. Experimental tests will be undertaken in Chapter 5 to further examine the effectiveness of proposed AVMD technique for nonlinear feature analysis and bearing fault detection.

Chapter 5

Experimental Tests and Results

This chapter will verify the effectiveness of the proposed AVMD technique, firstly by simulation test, and then by experiment tests. Its robustness will be examined by using data sets from another experimental setup.

5.1 Experimental Verification

Figure 5.1 shows the experimental setup used in this test. It is driven by a 3 HP induction motor with a speed range of 100 - 4200 rpm, controlled by a frequency converter (VFD022B21A). An elastic coupler is applied to eliminate high frequency vibrations generated by the motor. An optical sensor is used to provide a signal of one pulse per revolution to measure shaft speed. The accelerometer (ICP-603C01) in the smart DAQ system is mounted on top of the bearing to measure the vibration signal along the vertical axis. The tested bearing (MBER-10K) located on the left side of the housing is used for the test. The static bearing load is provided by two heavy mass discs and dynamic load is provided by a break system through a belt-drive.

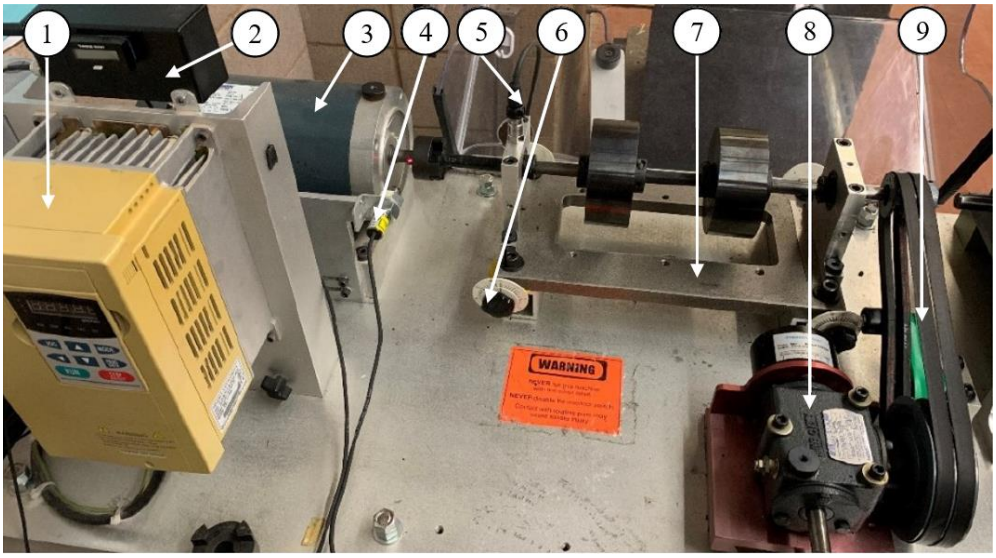

Figure 5.1: Experimental setup: (1) speed control; (2) encoder display; (3) drive motor; (4) optical encoder; (5) ICP accelerometer; (6) misalignment adjustor; (7) adjustable rig; (8) variable load system; (9) belt drive.

A series of data sets are collected under different speed and load conditions. A set of processing results from tests with 1800 rpm motor speed (or f_r = 30 Hz) and medium load level are used for illustration. The sampling frequency is 32,000 Hz, and the length of the signal is 100 k.

In this experiment, four bearing health conditions are considered for testing: a healthy bearing, a bearing with outer race fault, a bearing with inner race fault, and a bearing with rolling element defect. The tested bearings have the following parameters:

Rolling elements $Z = 8$,

Rolling element diameter $d = 7.938$ mm,

Pitch diameter $D = 33.503$ mm,

Contact angle $\theta = 0$ degrees.

Table 5.1 summarizes the characteristic frequencies in terms of shaft speed f_r Hz based on Eq.(1.1)-(1.3).

Table 5.1: Bearing fault frequencies in terms of shaft speed f_r Hz

Bearing Health Condition	Characteristic Frequency Hz
Healthy bearing	$f_H = f_r$
Outer race fault	$f_{od} = 3.0522 \times f_r$
Inner race fault	$f_{id} = 4.9477 \times f_r$
Rolling element fault	$f_{ed} = 3.9837 \times f_r$

For comparison, the test results of proposed AVMD method will compare with the following related techniques:

1) the Hilbert-Huang transform (HHT) [82] and
2) the Teager-Huang transform (THT) [83].

All the techniques are implemented in MATLAB 2022a.

5.1.1 Healthy Bearing Analysis

Figure 5.2 shows processing results using the related techniques, for the health bearing

with characteristic frequency f_H = 30 Hz. The AVMD is applied with K= 4 and penalty factor α = 1216 calculated using Eq. (4.19) as discussed in Chapter 4.

In this case, although all the related techniques can recognize the healthy bearing characteristic frequency and its few harmonics, the AVMD technique provide the most noticeable diagnostic results with highest magnitude compared with other two techniques.

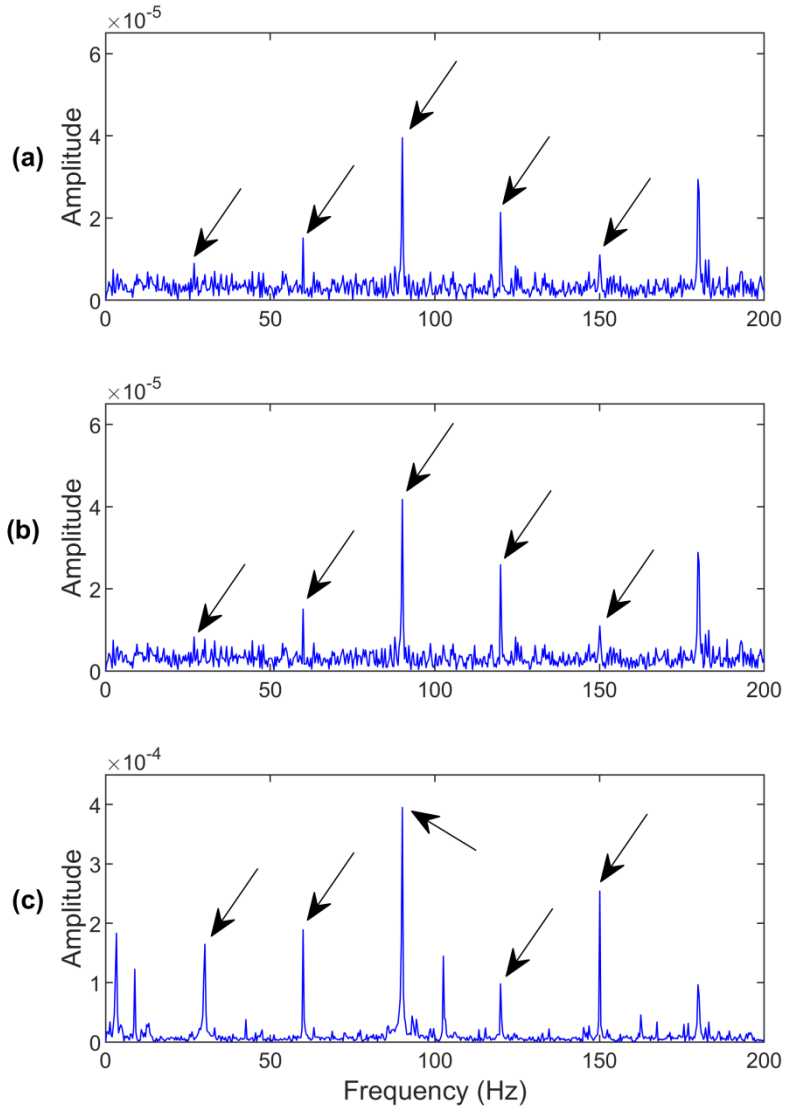

Figure 5.2: Processing results for a healthy bearing using the related techniques: (a) HHT, (b) THT, (c) AVMD. f_H = 30 Hz. Arrows specify characteristic frequency and its harmonics.

5.1.2 Outer-race Bearing Fault Detection

Figure 5.3 shows the processing results for a bearing with outer-race damage with a characteristic frequency f_{od} = 90.9 Hz. In this case, the AVMD technique uses K = 5 and

penalty factor α = 1216.

In this case, all the related techniques can recognize the outer race bearing fault characteristic frequency f_{od} = 90.9 Hz and its first few harmonics. This is because when the outer race is damaged, the generated impulses and features are time-invariant, which are easy to determine using general fault detection techniques. In this case, however, the fundamental characteristic frequency (f_{od} = 90.9 Hz) using the HHT in Figure 5.3(a) and the THT in Figure 5.3(b) is lower than an adjacent component in magnitude, which may generate false diagnostic result especially in automatic bearing health monitoring. On the other hand, the proposed AVMD technique can effectively suppress noise and predict the occurrence of outer race defect as demonstrated in Figure 5.3(c).

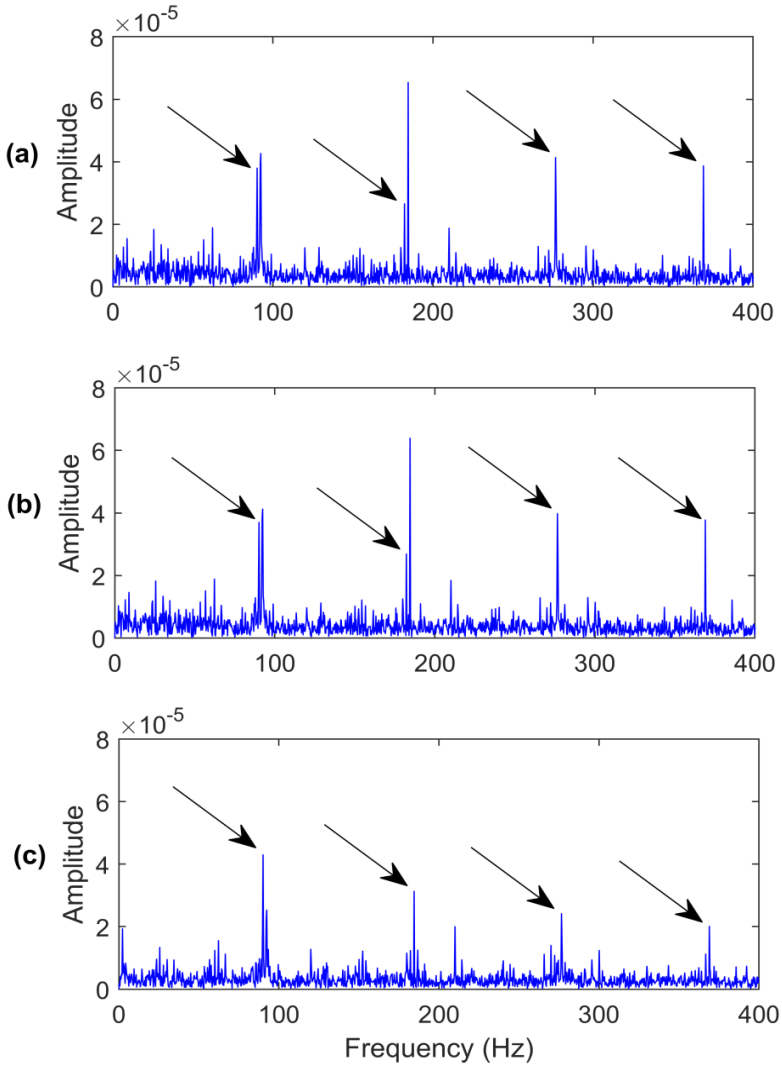

Figure 5.3: Processing results for an outer race damaged bearing using the related techniques: (a) HHT, (b) THT, (c) AVMD. f_{od} = 90.9 Hz. Arrows specify characteristic frequency and its harmonics.

5.1.3 Inner-race Bearing Fault Detection

Figure 5.4 shows the processing results using the related techniques for a bearing with inner race defect, with the characteristic frequency $f_{id} = 147.9$ Hz. In this case, the AVMD uses $K = 5$ and penalty factor $\alpha = 1304$.

In comparison of the HHT in Figure 5.4(a), the THT technique in Figure 5.4(b) provides better performance with clear fault detection with the domain fault characteristic frequency ($f_{id} = 147.9$ Hz) due to the advantage of Teager operator in signal demodulation. On the other hand, the proposed AVMD technique in Figure 5.4(c) outperforms even the THT with higher resolution, and can provide better fault diagnostic accuracy due to its efficient frequency suppression.

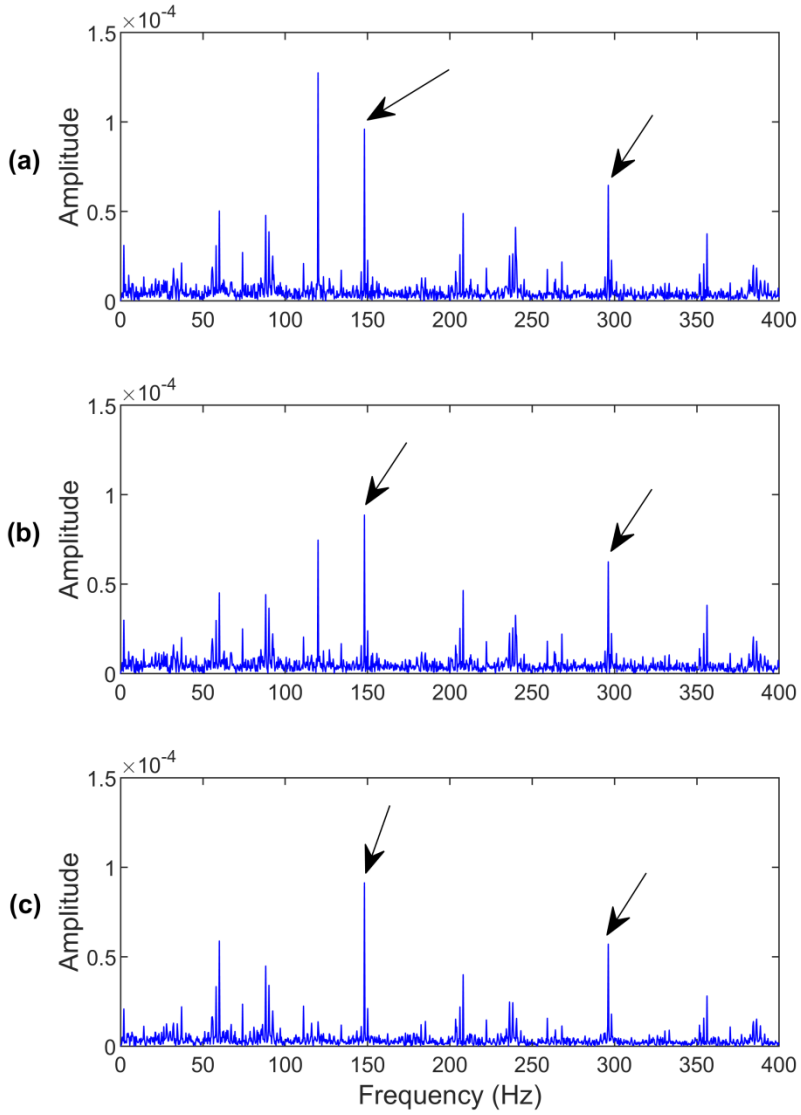

Figure 5.4: Processing results for an inner race damaged bearing using the related techniques: (a) HHT, (b) THT, (c) AVMD. f_{id} = 147.9 Hz. Arrows specify characteristic frequency and its harmonics.

5.1.4 Rolling-element Bearing Fault Detection

Figure 5.5 depicts the processing results for a bearing with the rolling element damage. The theoretical characteristic frequency is $f_{bd} = 91.57$ Hz. The AVMD has parameters of K = 5 and penalty factor α = 284.

In this case, none of these three techniques can provide clear fault detection results. In general, fault detection in rolling element is a challenging task as the representative features could be time-varying. Both the HHT (Figure 5.5(a)) and THT (Figure 5.5(b)) have failed to identify the characteristic fault frequency ($f_{bd} = 91.57$ Hz). The AVMD is the only technique

that can recognize the fundamental fault characteristic frequency in Figure 5.5(c), even though it is not the dominant frequency component in the spectral map.

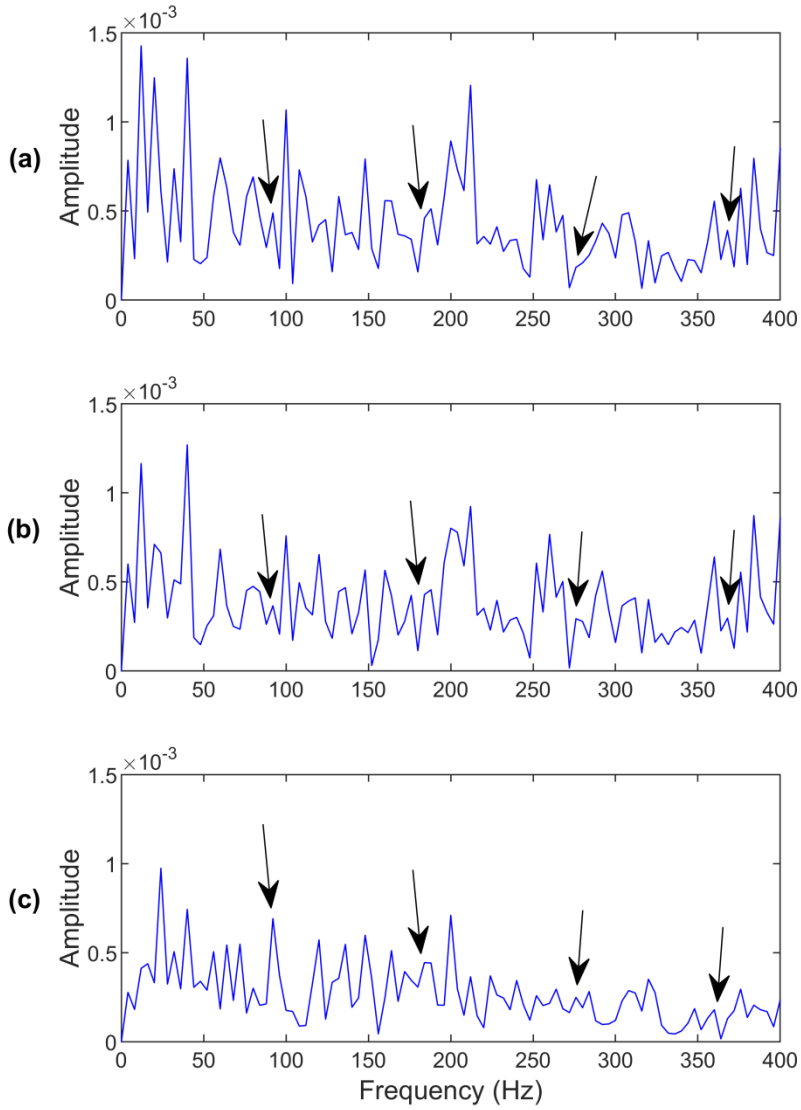

Figure 5.5: Processing results for a rolling element damaged bearing using the related techniques: (a) HHT, (b) THT, (c) AVMD. f_{bd} = 91.57 Hz. Arrows specify characteristic frequency and its harmonics.

5.2 Robustness Verification

The robustness of the proposed AVMD technique will examined in this section by using data sets from online database of Case Western Reserve University (CWRU) Bearing Data Center [84]. As shown in Figure 5.6, this experimental setup is driven by a 2-HP drive motor. The load is provided by the load motor on the right. The tested bearing is in the bearing housing between the two motors. The tested bearing model is 6205-2RS JEM SKF (deep

groove ball bearing from SKF) [85], which has the following parameters:

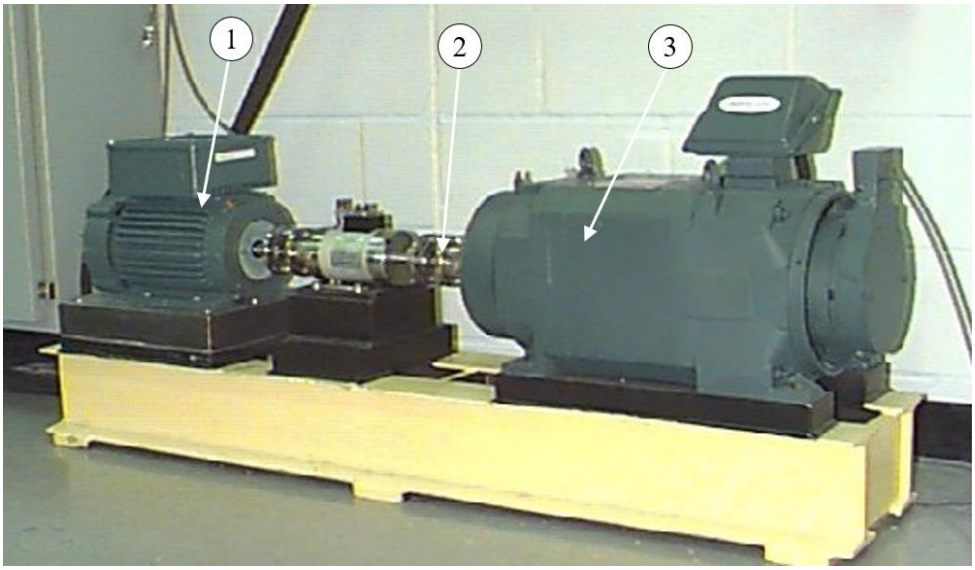

Figure 5.6: CWRU bearing test experiment setup [85]: (1) drive motor, (2) tested bearing, (3) load motor.

Rolling elements $Z = 8$;

Rolling element diameter $d = 7.94$ mm;

Pitch diameter $D = 39.04$ mm;

Contact angle $\theta = 0$ degrees.

A set of data sets are selected with motor speed of 1750 rpm or 29.17 Hz, and medium load level of 2.0 HP for evaluation. The sampling frequency is 48 kHz, and the signal length is 100 k.

Similarly, four bearing health conditions are considered for testing: healthy bearing, bearing with outer race fault, bearing with inner race fault, and bearing with rolling element defect. Table 5.2 summarizes the characteristic frequencies in terms of shaft speed f_r for the tested bearing under different health conditions, which are calculated using Eq. (1.1)-(1.3). Similarly, the performance of the proposed AVMD technique will be compared with the HHT and the THT techniques as well. All the techniques are implemented in MATLAB 2022a.

Table 5.2: Bearing fault frequencies for the CWRU data center experiment setup.

Bearing condition	Shaft Speed f_r Hz
Healthy bearing	$f_H = f_r$
Outer-race fault	$f_{od} = 3.5848 \times f_r$
Inner-race fault	$f_{id} = 5.4152 \times f_r$
Rolling-element fault	$f_{ed} = 4.7135 \times f_r$

5.2.1 Healthy Bearing Analysis

Figure 5.7 shows the processing results using the related techniques for a healthy bearing, with the characteristic frequency $f_H = 29.17$ Hz. The AVMD uses parameter of K= 4 and penalty factor $\alpha = 434$.

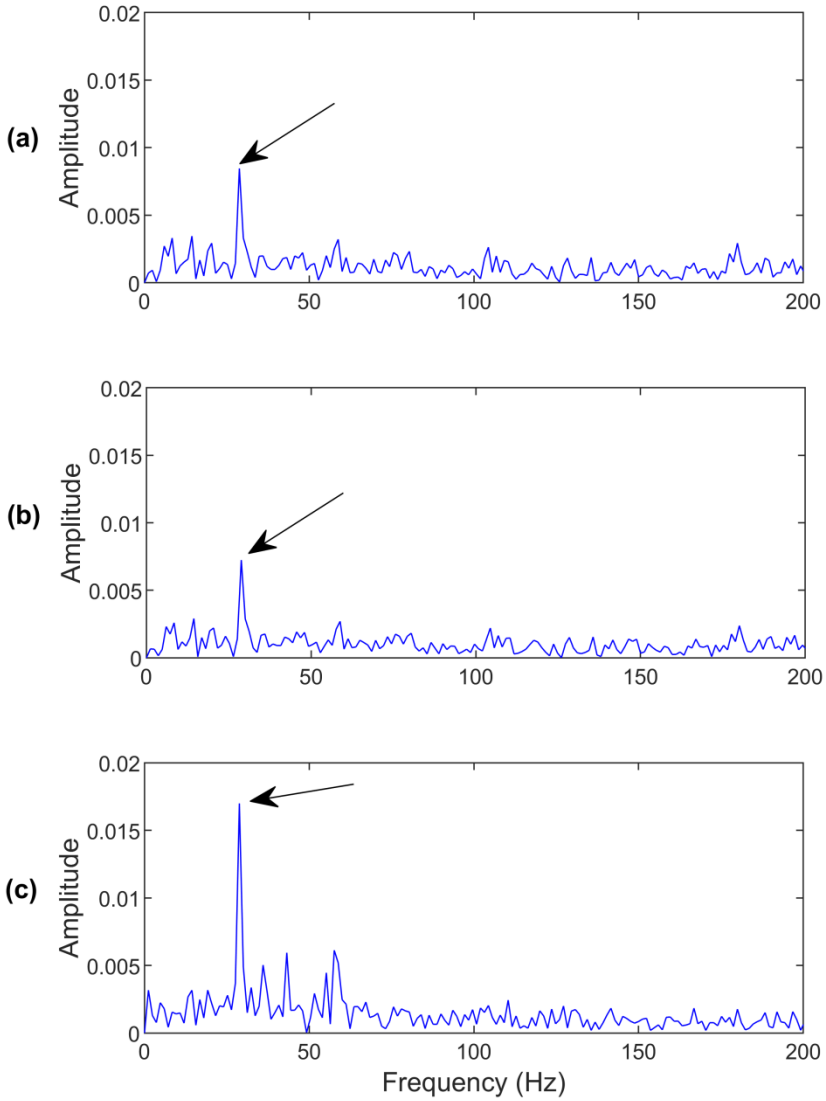

Figure 5.7: Processing results for a healthy bearing using the related techniques: (a) HHT, (b) THT, (c) AVMD. f_H = 29.17 Hz. Arrows specify characteristic frequency.

In this case, all three techniques can recognize the health condition of the bearing with clear characteristic frequency and its harmonics. However, the proposed AVMD technique can provide the best performance compared to the other two techniques with the highest resolution.

5.2.2 Outer-race Bearing Fault Detection

Figure 5.8 shows the processing results for a bearing with an outer race fault, with the characteristic frequency f_{od} = 104.56 Hz. The AVMD parameters are K = 5 and penalty factor α = 1021.

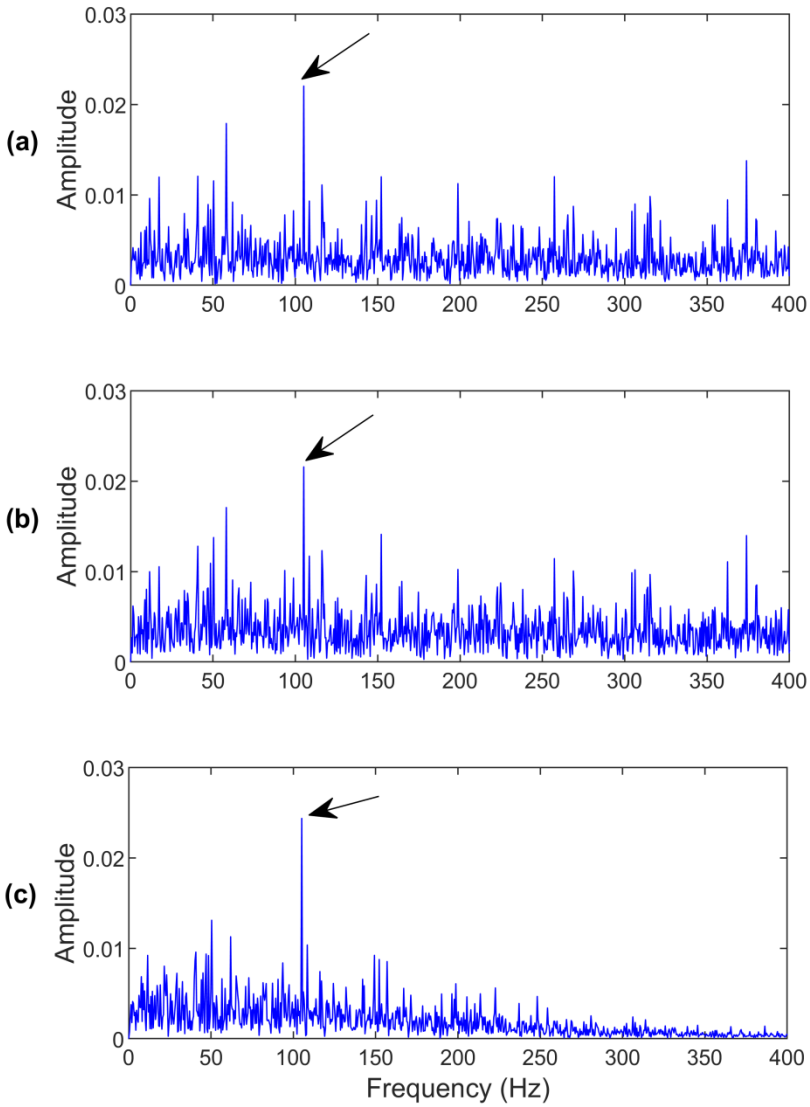

Figure 5.8: Processing results for an outer-race damaged bearing using the related techniques: (a) HHT, (b) THT, (c) AVMD. f_{od} = 104.56 Hz. Arrows specify characteristic frequency.

In this case, all the related techniques can recognize the outer race bearing fault with clear characteristic frequency and harmonics. The AVMD technique (Figure 5.8(c)), however, can provide higher resolution with lower noise than the HHT and THT techniques, due to its efficient training and noise suppression.

5.2.3 Inner-race Bearing Fault Detection

Figure 5.9 shows comparison of the processing results using the related techniques for a bearing with the inner-race damage, with the characteristic frequency f_{id} = 156.14 Hz. The AVMD is applied with K = 5 and penalty factor α = 1034.

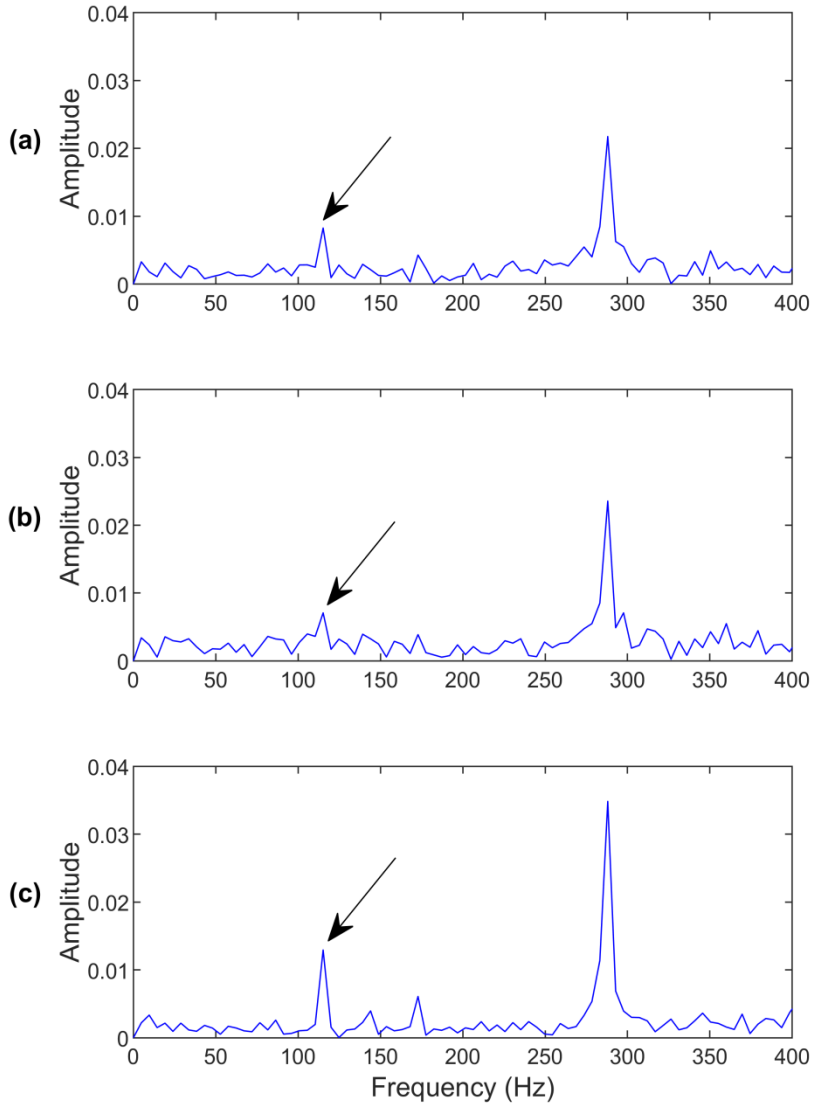

Figure 5.9: Processing results for an inner-race damaged bearing using the related techniques: (a) HHT, (b) THT, (c) AVMD. f_{id} = 147.9 Hz. Arrows specify characteristic frequency and its harmonics.

In this case, none of these three techniques can provide clear diagnostic result with a dominant characteristic frequency. However, the AVMD technique (Figure 5.9(c)) outperforms another two techniques in identifying the fault characteristic frequency with higher magnitude (resolution).

5.3.4 Rolling-element Bearing Fault Detection

Figure 5.10 shows processing results of these three techniques for a bearing with the rolling element damage, with the characteristic frequency $f_{bd} = 131.32$ Hz. The AVMD has parameters $K = 5$ and penalty factor $\alpha = 431$.

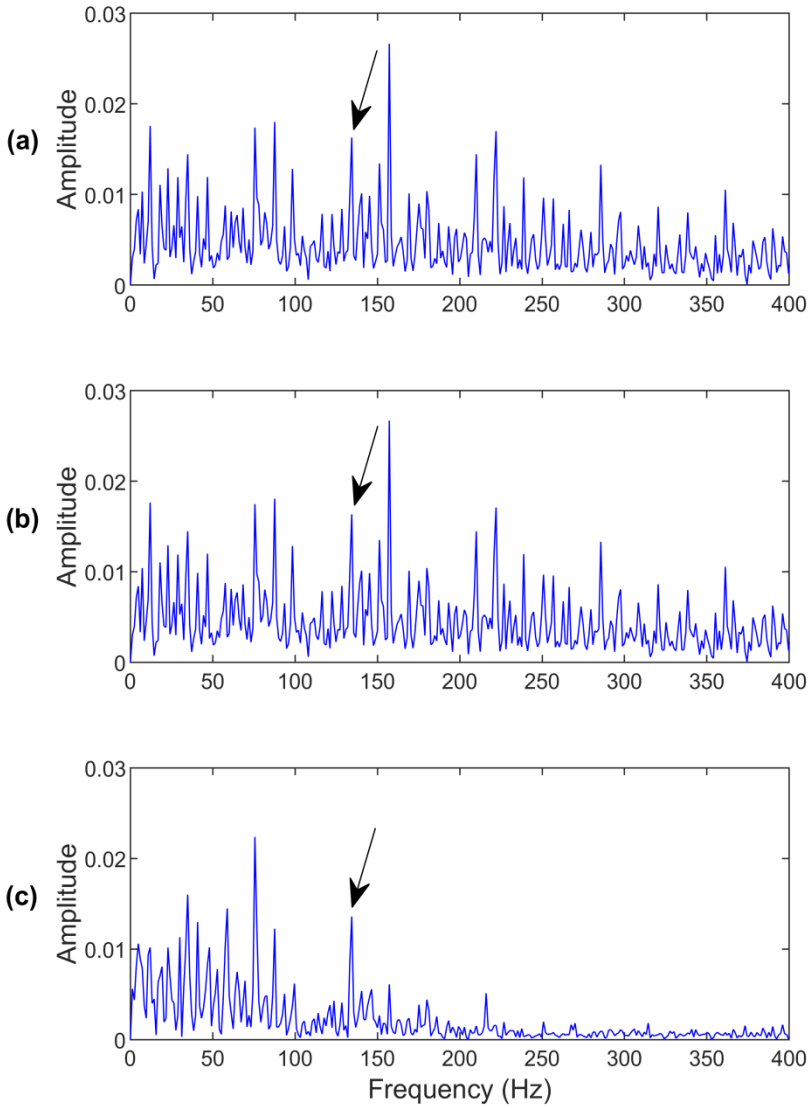

Figure 5.10: Processing results for a rolling-element damaged bearing using the related techniques: (a) HHT, (b) THT, (c) AVMD. f_{bd} = 131.32 Hz. Arrows specify characteristic frequency.

In this case, all three techniques cannot provide reliable fault diagnosis without recognizing dominant fault characteristic frequency components; it is because the rolling element fault related features are time-varying. However, the AVMD technique can still provide the best prediction due to its noise suppression especially beyond 100 Hz.

5.3 Summary

In this chapter, the effectiveness of proposed AVMD technique has been verified by experimental tests. The tested bearing conditions include healthy bearings and bearings with outer race fault, inner race defect and rolling element damage. The tests are performed under

different load and speed conditions. The effectiveness of the proposed AVMD technique is examined with the comparison of other related signal processing techniques. Its robustness is verified by using data sets from Case Western Reserve University. From the systematic testing, it is shown that the proposed AVMD technique outperforms other related techniques under these controlled testing conditions. However, its performance still needs to be improved in some time-varying cases such as diagnosis of rolling element fault.

Chapter 6

Conclusions and Future Work

6.1 Conclusion

Rolling element bearings are commonly used in rotating machinery. On the other hand,, bearings are also the most easily damaged components. Efficient bearing health condition monitoring and diagnosis is an important aspect to optimal equipment management and predictive maintenance in modern industry. However reliable bearing fault detection still remains a challenging task in research and development, because bearing fault related features could vary with bearing dynamics and operating conditions. To tackle these problems, the first objective of this research is to develop a high-speed and high-resolution DAQ system to collect vibration signals. The second objective is to propose an adaptive Variational Mode Decomposition (AVMD) technique for non-stationary signal analysis and bearing fault detection.

Firstly, a recursive trigonometric (RT) technique has been proposed to develop an FPGA-based sinusoidal waveform generator. The general capability of Cyclone IV E family FPGA has been investigated for the algorithm implementation. In addition, the proposed RT technique is used to optimize the trigonometric waveforms generated in hardware. Its effectiveness has been examined by both simulation and hardware tests. Test results have verified the accuracy of the proposed RT technique over the related techniques.

Secondly, a MCU-based DAQ system is developed for vibration signal collection. Signal conditioning functions, high-resolution ADC functions, high-speed data transfer, control software, and user graphical interface are designed and implemented for the DAQ system.

Thirdly, a new AVMD technique has been proposed for nonlinear signal analysis and bearing fault detection. The AVMD takes several procedures in signal processing: 1) The VMD method is used to compute the correlation between the original signal and the synthesis of the decomposed modes. 2) The penalty factor is determined analytically for each mode analytically. 3) Ensemble kurtosis is computed for each mode. 4) The optimal sub-mode is

selected, and the corresponding envelope analysis is undertaken for bearing fault detection. The effectiveness of the proposed AVMD technique is verified by both simulation and experimental tests under different bearing health and operating conditions. Its robustness is verified by tests using datasets from a different test apparatus (online data). The test results have shown that the proposed AVMD technique can properly denoise the signal and highlight the fault-related features for bearing fault detection. It outperforms the related techniques under these controlled testing conditions. It has potential to be used for bearing health condition monitoring in real industrial applications.

6.2 Future Work

The following advanced R&D work will be undertaken in the future:

(1) The FPGA-based DAQ system will be design and implemented for high speed and more accuracy data collection from water pump stations in the Bare Point Water Treatment Plant in Thunder Bay, Ontario.

(2) The MCU-based DAQ system will be improved for high-speed wireless data transmission by using different transmission protocols. The DAQ software will be improved to facilitate different control operations, and to enhance robustness under different software/hardware environment and conditions.

(3) New analytical method will be proposed to optimize VMD parameters and improve the AVMD algorithm for more reliable remote bearing health monitoring.

Reference

[1] D. Neupane and J. Seok, “Bearing Fault Detection and Diagnosis Using Case Western Reserve University Dataset With Deep Learning Approaches: A Review,” *IEEE Access,* vol. 8, pp. 93155-93178, 2020.

[2] W. T. Thomson and M. Fenger, “Current signature analysis to detect induction motor faults,” *IEEE Industry Applications Magazine*, vol. 1, pp. 25-33, 2001.

[3] SKF, “6203 Deep groove ball bearing,” SFK.com, https://www.skf.com/group/products/rolling-bearings/ball-bearings/deep-groove-ball-bearings/productid-6203 (accessed Aug. 22, 2022).

[4] W. Wang, “Analysis of Fault Detection in Rolling Element Bearings,” *IEEE Instrumentation and Measurement Magazine*, vol. 24, no. 3, pp. 42-49, 2021.

[5] SFK, “Bearing damage and failure analysis,” SFK.com, https://www.skf.com/binaries/pub12/ (accessed Aug. 22, 2022).

[6] S. Lu, P. Zheng, Y. Liu, et al, “Sound-aided vibration weak signal enhancement for bearing fault detection by using adaptive stochastic resonance,” *Journal of Sound and Vibration*, vol. 449, pp. 18-29, 2019.

[7] P. Zhang, S. Liu, A. Tao, J. Cheng and P. Gao, “Afault diagnosis method based on low signal to noise ratio vibration measurement for use in casing cutters,” *Measurement Science and Technology*, vol. 33, no. 4, 2022.

[8] G. Meijer, Smart Sensor Systems, Chichester: J. Wiley & Sons, 2008.

[9] W. Wang and O. A. Jianu, “A smart sensing unit for vibration measurement and monitoring,” *IEEE/ASME Transactions on Mechatronics*, vol. 15, no. 1, pp. 70-79, 2010.

[10] A. Morris and R. Langari, Measurement and Instrumentation Theory and Application, San Diego: Academic Press, 2015.

[11] J. M. Landgraf, M. J. LeVine, A. J. Ljubicic, J. M. Nelson, D. Padrazo and M. W. Schulz, “An overview of the STAR DAQ system,” *Nuclear Instruments and Methods in Physics Research Section A: Accelerators, Spectrometers, Detectors and Associated Equipment*, vol. 499, no. 2, pp. 762-765, 2003

[12] S. K., Mitra, Digital Signal Processing: A Computer-Based Approach. New York, NY:

McGraw-Hill, 1998.

[13] G. M. Smith, “Data Acqusition,” Dewesoft.com, https://dewesoft.com/daq/what-is-data-acquisition#data-storage (accessed Aug. 22, 2022)

[14] Y. Kim, Y. Park and J. Choi, “A study on the adoption of IoT smart home service: using Value-based Adoption Model,” *Total Quality Management & Business Excellence*, vol. 28, no. 9, pp. 1149-1165, 2017.

[15] H. Jo and Y. I. Yoon, “Intelligent smart home energy efficiency model using artificial Tensor Flow engine,” *Human-centric Computing and Information Sciences*, vol. 8, no. 9, 2018.

[16] L. Hou and N. W. Bergmann, “Novel Industrial Wireless Sensor Networks for Machine Condition Monitoring and Fault Diagnosis,” *IEEE Transactions on Instrumentation and Measurement*, vol. 61, no. 10, pp. 2787-2798, 2012.

[17] National Instrument, “USB-6009 Multifunction I/O Device,” NI.com, https://www.ni.com/en-ca/support/model.usb-6009.html (accessed Aug. 22, 2022).

[18] T. Sengoz, “Online condition monitoring and fault detection in induction,” M.S.thesis, Lakehead University, Thunder Bay, ON, Canada, 2017. [Online]. Available: https://knowledgecommons.lakeheadu.ca/

[19] Z. Cheng, “An enhanced Teager Huang transform technique for bearing fault detection,” M.S.thesis, Lakehead University, Thunder Bay, ON, Canada, 2021. [Online]. Available: https://knowledgecommons.lakeheadu.ca/

[20] T. D. Toky, “An Adaptive Neuro Fuzzy Classifier for Bearing Fault Diagnosis,” M.S.thesis, Lakehead University, Thunder Bay, ON, Canada, 2022. [Online]. Available: https://knowledgecommons.lakeheadu.ca/

[21] P. Yan, C. Yan, K. Wang, F. Wang and L. Wu, “5-DOF Dynamic Modeling of Rolling Bearing with Local Defect considering Comprehensive Stiffness under Isothermal Elastohydrodynamic Lubrication,” *Shock and Vibration*, vol. 2020, 2020.

[22] T. Williams, X. Ribadeneria and S. Billingtons, “Rolling element bearing diagnostics in run-to-failure lifetime testing,” *Mechanical System and Signal Processing*, vol. 15, no. 5, pp. 979-993, 2001.

[23] T. Sengoz, Z. Chen and W. Wang, “A Teager-Kaiser Spectrum Technique for Bearing Fault Detection in Induction Motors,” *International Journal of Mechanical and Mechatronics Engineering*, vol. 10, no. 5, pp. 18-24, 2019.

[24] N. Tandon and B. C. Nakra, “Detection of defects in rolling element bearing by vibration monitoring,” *Journal, Mechanical Engineering Division*, vol. 73, pp. 271-282, 1993.

[25] D. Dyer and R. M. Stewart, “Detection of rolling element bearing damage by statistical vibration analysis,” *Journal of Mechanical Design*, vol. 100, no. 2, pp. 229-235, 1978.

[26] R. Dwyer, “Detection of non-Gaussian signals by frequency domain Kurtosis estimation,” *IEEE International Conference on Acoustics, Speech, and Signal Processing*, Boston, 1983.

[27] A. Shrivastava and S. Wadhwani, “Development of fault detection system for ball bearing of induction motor using vibration signal,” *International Journal of Scientific Research*, vol. 2, no. 5, pp. 256-259, 2012.

[28] V. K. Rai and A. R. Mohanty, “Bearing fault diagnosis using FFT of intrinsic mode functions in Hilbert–Huang transform,” *Mechanical Systems and Signal Processing*, vol. 21, no. 6, pp. 2607-2615, 2007.

[29] S. Fu, K. Liu, Y. Xu and Y. Liu, “Rolling Bearing Diagnosing Method Based on Time Domain Analysis and Adaptive Fuzzy C-Means Clustering,” *Shock and Vibration*, vol. 2016, 2016.

[30] E. Sejdic, I. Djurovic and J. Jiang, “Time–frequency feature representation using energy concentration: An overview of recent advances,” *Digital Signal Processing*, vol. 19, pp. 153-183, 2009.

[31] M. Cocconcelli, R. Zimroz, R. Rubini and W. Bartelmus, “STFT based approach for ball bearing fault detection in a varying speed motor,” *Condition Monitoring of Machinery in Non-Stationary Operations*, Berlin, 2012.

[32] J. H. Lee, J. Kim and H. J. Kim, “Development of enhanced Wigner-Ville distribution function,” *Mechanical Systems and Signal Processing*, vol. 15, no. 2, pp. 367-398, 2001.

[33] Y. Yang, D. Yu and J. Cheng, “A roller bearing fault diagnosis method based on EMD energy entropy and ANN,” *Journal of Sound and Vibration*, vol. 294, pp. 269-277, 2006.

[34] S. Osman and W. Wang, “An enhanced Hilbert-Huang transform technique for bearing,” *Measurement Science and Technology*, vol. 24, no. 8, 2013.

[35] X. Zhang, Z. Liu, Q. Miao and L. Wang, “Bearing fault diagnosis using a whale optimization algorithm-optimized orthogonal matching pursuit with a combined time–frequency atom dictionary,” *Mechanical Systems and Signal Processing*, vol. 107, pp. 29-42, 2018.

[36] Z. K. Peng, P. W. Tse and F. L. Chu, “A comparison study of improved Hilbert–Huang transform and wavelet transform: Application to fault diagnosis for rolling bearing,” *Mechanical Systems and Signal Processing*, vol. 19, no. 5, pp. 974-988, 2005.

[37] J. Gao and P. Shang, “Analysis of complex time series based on EMD energy entropy plane,” *Nonlinear Dynamics*, vol. 96, pp.465-482, 2019.

[38] X. Zhang, Q. Miao, H. Zhang and L. Wang, “A parameter-adaptive VMD method based on grasshopper optimization algorithm to analyze vibration signals from rotating machinery,” *Mechanical Systems and Signal Processing*, vol. 108, pp. 58-72, 2018.

[39] S. Aggarwal, P. K. Meher and K. Khare, “Scale-Free Hyperbolic CORDIC Processor and Its Application to Waveform Generation,” *IEEE Transactions on Circuits and Systems I: Regular Papers*, vol. 60, no. 2, pp. 314-326, 2013.

[40] Y. Cheng, Y. Lei, Y. Peng, T. He and Z. Deng, “Configurable Floating-Point FFT Accelerator on FPGA Based Multiple-Rotation CORDIC,” *Chinese Journal of Electronics*, vol. 25, no. 6, pp. 1063-1070, 2016.

[41] B. Zhu, Y. Lei, Y. Peng and T. He, “Low Latency and Low Error Floating-Point Sine/Cosine Function Based TCORDIC Algorithm,” *IEEE Transactions on Circuits and Systems I: Regular Papers*, vol. 64, no. 4, pp. 892-905, 2017.

[42] S. E. Turner, R. T. Chan and J. T. Feng, “ROM-Based Direct Digital Synthesizer at 24 GHz Clock Frequency in InP DHBT Technology,” *IEEE Microwave and Wireless Components Letters*, vol. 18, no. 8, pp. 566-568, 2008.

[43] P. K. Meher, J. Valls, T. Juang, K. Sridharan and K. Maharatna, “50 Years of CORDIC: Algorithms, Architectures, and Applications,” *IEEE Transactions on Circuits and Systems I: Regular Papers*, vol. 56, no. 9, pp. 1893-1907, 2009.

[44] F. J. Jaime, M. A. Sanchez, J. Hormigo, J. Villalba and E. L. Zapata, "Enhanced Scaling-Free CORDIC," *IEEE Transactions on Circuits and Systems I: Regular Papers*, vol. 57, no. 7, pp. 1654-1662, 2010.

[45] K. Maharatna, S. Banerjee, E. Grass, M. Krstic and A. Troya, "Modified virtually scaling-free adaptive CORDIC rotator algorithm and architecture," *IEEE Transactions on Circuits and Systems for Video Technology*, vol. 15, no. 11, pp. 1463-1474, 2005.

[46] S. Aggarwal, P. K. Meher and K. Khare, "Concept, Design, and Implementation of Reconfigurable CORDIC," *IEEE Transactions on Very Large Scale Integration (VLSI) Systems*, vol. 24, no. 4, pp. 1588-1592, 2016.

[47] E. Monmasson and M. N. Cirstea, "FPGA Design Methodology for Industrial Control Systems—A Review," *IEEE Transactions on Industrial Electronics*, vol. 54, no. 4, pp. 1824-1842, 2007.

[48] National Instrument, "FPGA Fundamentals," NI.com. https://www.ni.com/en-ca/innovations/white-papers/08/fpga-fundamentals.html#section-20661164 (accessed Aug. 22, 2022).

[49] S. Brown, "FPGA architectural research: A survey," *IEEE Design and Test of Computers*, vol. 13, no. 4, pp. 9-15, 1996.

[50] S. lokhandwala, "Top 10 FPGA Companies," fpganinjas.io. https://fpganinjas.io/top-10-list-of-fpga-companies/ (accessed Aug. 22, 2022).

[51] Digikey, "EP4CE15F23C8", Digikey.ca. https://www.digikey.ca/en/products/detail/intel/EP4CE15F23C8/2288296 (accessed Aug. 22, 2022).

[52] Analog Device, "AD9707 Datasheet," Analog.com. https://www.analog.com/en/products/ad9707.html (accessed Aug. 22, 2022).

[53] R. Shula and K. C. Ray, "Low latency hybrid CORDIC algorithm," *IEEE Transactions on Computers*, vol. 63, no. 12, pp. 3066-3078, 2013.

[54] J. Villalba, J. C. Arrabal, E. L. Zapata, E. Antelo and J. D. Bruguera, "Radix-4 vectoring CORDIC algorithm and architectures," *Journal of VLSI signal processing systems for signal, image and video technology*, vol. 19, no. 2, pp. 127-147, 1998.

[55] M. Garrido, P. Källström, M. Kumm and O. Gustafsson, “CORDIC II: A New Improved CORDIC Algorithm,” *IEEE Transactions on Circuits and Systems II: Express Briefs*, vol. 63, no. 2, pp. 186-190, 2016.

[56] “IEEE Standard for Verilog Hardware Description Language,” in *IEEE Std 1364-2005(Revision of IEEE Std 1364-2001)*,pp.1-590, 2006.

[57] Intel, “Intel® Quartus® Prime Software,” Intel.com. https://www.intel.com/content/www/us/en/products/details/fpga/development-tools/quartus-prime.html (accessed Aug. 22, 2022).

[58] PCB PIEZOTRONICS, “603C01 datasheet,” PCB.com https://www.pcb.com/products?m=603c01(accessed Aug. 22, 2022).

[59] Wilcoxon, “Piezovelocity transducers,” Wilcoxon.com. https://wilcoxon.com/wp-content/uploads/2016/07/TN18_Industrial-vibration-sensor-selection-PVTs.pdf (accessed Aug. 22, 2022).

[60] DURACELL, “9V Battery,” duracell.com https://www.duracell.com/en-us/products/9v/ (accessed Aug. 22, 2022).

[61] Texas Instruments, “MC34063A Datasheet,” ti.com. https://www.ti.com/product/MC34063A(accessed Aug. 22, 2022).

[62] Texas Instruments, “LM334 Datasheet,” ti.com. https://www.ti.com/product/LM334(accessed Aug. 22, 2022).

[63] Analog Devices, “OP07 Datasheet,” ti.com. https://www.analog.com/en/products/op07.html (accessed Aug. 22, 2022).

[64] Texas Instruments, “ADS131A04 datasheet,” ti.com. https://www.ti.com/product/ADS131A04 (accessed Aug. 22, 2022).

[65] ESPRESSIF, “ESP32-S2,” espressif.com. https://www.espressif.com/en/products/socs/esp32-s2 (accessed Aug. 22, 2022).

[66] VISHAY, “IRF520 datasheet,” vishay.com. https://www.vishay.com/docs/91017/irf520 (accessed Aug. 22, 2022).

[67] K. Dragomiretskiy and D. Zosso, “Variational Mode Decomposition,” *IEEE Transactions on Signal Processing*, vol. 62, no. 3, pp. 531-544, 2014.

[68] R. T. Rockafellar , “A dual approach to solving nonlinear programming problems by unconstrained optimization,” *Mathematical Programming*, vol. 5, pp. 354-373, 1973.

[69] Y. Miao, M. Zhao and J. Lin, “Identification of mechanical compound-fault based on the improved parameter-adaptive variational mode decomposition,” *ISA Transcations*, vol. 84, pp. 82-95, 2019.

[70] G. Zhang, H. Liu, J. Zhang, Y. Yan, L. Zhang, C. Wu, X. Hua and Y. Wang, “Wind power prediction based on variational mode decomposition,” *Journal of Modern Power Systems and Clean Energy*, vol. 7, no. 2, pp. 281-288, 2019.

[71] Q. Chen, S. Dai and H. Dai, “A Rolling Bearing Fault Diagnosis Method Based on EMD and Quantile Permutation Entropy,” *Mathematical Problems in Engineering*, vol. 2019, 2019.

[72] Y. Liu, Y. Chai, B. Liu and Y. Wang, “Impulse Signal Detection for Bearing Fault Diagnosis via Residual-Variational Mode Decomposition,” *Applied Science*, vol. 11, no. 7, pp. 30-53, 2021.

[73] J. Li, X. Yao, H. Wang and J. Zhang, “Periodic impulses extraction based on improved adaptive VMD and sparse code shrinkage denoising and its application in rotating machinery fault diagnosis,” *Mechanical Systems and Signal Processing*, vol. 126, pp. 568-589, 2019.

[74] G. Tang, W. Hou, H. Wang, G. Luo and J. Ma, “Compressive Sensing of Roller Bearing Faults via Harmonic Detection from Under-Sampled Vibration Signals,” *Sensors (Basel)*, vol. 15, no. 10, pp.25648-25662, 2015.

[75] J. J. A. Moors, “The meaning of kurtosis: Darlington reexamined,” *The American Statistician*, vol. 40, no. 4, pp. 283-284, 1986.

[76] S. Zhu, H. Xia, B. Peng, E. Zio, Z. Wang and Y. Jiang, "Feature extraction for early fault detection in rotating machinery of nuclear power plants based on adaptive VMD and Teager energy operator," Annals of Nuclear Energy, vol. 160, 2021.

[77] MathWorks, “Envelope spectrum for machinery diagnosis,” mathworks.com. https://www.mathworks.com/help/signal/ref/envspectrum.html (accessed Aug. 22, 2022).

[78] C. Yi, H. Wang, L. Ran, L. Zhou and J. Lin, “Power spectral density-guided variational

mode decomposition for the compound fault diagnosis of rolling bearings," *Measurement*, vol. 199, 2022.

[79] B. Xu, F. X. Zhou, H. Li, B. Yan and Y. Liu, "Early fault feature extraction of bearings based on Teager energy operator and optimal VMD," *ISA Transactions*, vol. 86, pp. 249-265, 2019.

[80] P. Zhang and J. Yan, "Fault Feature Extraction of Wind Turbine Rolling Bearing Based on PSO-VMD," *in Proceedings of 2019 Chinese Intelligent Automation Conference*, Singapore, 2019.

[81] W. Xu and J. Hu, "A Novel Parameter-Adaptive VMD Method Based on Grey Wolf Optimization with Minimum Average Mutual Information for Incipient Fault Detection," *Shock and Vibration*, vol. 2021, 2021

[82] N. Huang, "The empirical mode decomposition and the Hilbert spectrum for nonlinear," *Proceedings of the Royal Society of London. Series A: Mathematical, Physical and Engineering Sciences*, vol. 454, no. 1971, pp. 903-995, 1998.

[83] H. Li, Y. Zhang and H. Zheng, "Bearing fault detection and diagnosis based on order tracking and Teager-Huang transform," *Journal of Mechanical Science and Technology*, vol. 24, no. 3, pp. 811-822, 2010.

[84] Case Western Reserve University, "Bearing Data Center," engineering.case.edu. https://engineering.case.edu/bearingdatacenter (accessed Aug. 22, 2022).

[85] SKF, "6205 Deep groove ball bearing," SFK.com, https://www.skf.com/group/products/rolling-bearings/ball-bearings/deep-groove-ball-bearings/productid-6205 (accessed Aug. 22, 2022).